CORA Cork Open Research Archive
Cartlann Taighde Oscailte Chorcaí

Title	Flow underlying coupled surface and internal waves
Authors	Henry, David;Villari, Gabriele
Publication date	2021-11-17
Original Citation	Henry, D. and Villari, G. (2022) 'Flow underlying coupled surface and internal waves', Journal of Differential Equations. Journal of Differential Equations, 310, pp. 404–442. doi: 10.1016/j.jde.2021.11.009.
Type of publication	Article (peer-reviewed)
Link to publisher's version	https://www.sciencedirect.com/science/article/pii/S0022039621006987 - 10.1016/j.jde.2021.11.009
Rights	https://creativecommons.org/licenses/by-nc-nd/4.0/
Download date	2026-11-06 02:16:13
Item downloaded from	https://hdl.handle.net/10468/12520

UCC
University College Cork, Ireland
Coláiste na hOllscoile Corcaigh

Flow underlying coupled surface and internal waves

David Henry Gabriele Villari

Abstract

In this article we investigate the underlying fluid motion induced by internal water waves, coupled with surface waves, in a two fluid layer model. We employ a phase-plane approach to achieve a detailed Eulerian description of the underlying wave-field kinematics for linear travelling waves. Additionally, the qualitative motion of individual fluid particles is established by way of a Lagrangian analysis of the appropriate nonlinear dynamical systems.

Keywords: Internal waves; Surface waves; Particle trajectories; Phase portraits.
AMS Subject Classification (2020): P35Q35, 76B15, 37N10, 70K05.

1 Introduction

Internal water waves are particularly interesting, and challenging, from both the mathematical and physical viewpoints. They arise where there is a jump in density between fluid layers, which may occur in an oceanographical context due to variations in temperature, salinity, or other fluctuations in the equations of state. The density structure of the ocean can, in many instances, be represented by two fluid-layer models, in which case the dividing interface is called a pycnocline (also known as a thermocline if the density difference is primarily due to temperature variations). Internal waves may be generated by tidal forces, the action of a wind, or pressure fluctuation. At a localised level, ships may cause internal waves if there is a shallow, brackish upper layer (as is prevalent in glacial coastal regions and fjords) leading to the so-called 'dead water' phenomenon. Overviews, surveys and references pertaining to recent research into internal wave motion (ranging from applied to purely theoretical considerations) can be found in [10, 13, 18, 20, 32, 41].

Internal waves play a fundamental role in any meaningful description of large-scale ocean dynamics [10, 19, 43]. However, by their nature and location, they are inherently difficult to observe and measure [18, 20, 32]. This difficulty in obtaining experimental and field data further amplifies the relevance of pursuing theoretical investigations into their motion. Of course, accommodating wave motion at both an internal interface, coupled with the free surface, significantly magnifies the complexity of an already intractable mathematical problem: we do not adopt the classical 'rigid-lid', or infinite fluid domain, approximations that are commonly employed when modelling internal waves.

Determining the underlying fluid motion generated by a wave propagating on an interface is an intriguing area of mathematical research which has important practical implications in the broad field of fluid mechanics. From a theoretical perspective, water waves are a subject of immense difficulty and complexity due to the intractability of the governing equations to mathematical analysis. However, recent mathematical advances have enabled researchers to make substantial progress in this field (cf. the discussions and references in [4, 6, 33]). In the past decade or so, fine properties of the underlying flow for periodic travelling surface water waves have been determined using various techniques from mathematical analysis and differential equations. It has been proven, both in the approximate linear regime [7, 12, 17, 22, 23, 27, 28, 29, 36, 37], and for exact solutions of the fully nonlinear governing equations [3, 5, 8, 21, 24, 25, 35, 40], that fluid particle paths are uniformly non-closed throughout the fluid domain. These results have conclusively disproved the long-held supposition that fluid particles follow closed trajectories for linear (small-amplitude) surface wave motion [4, 31, 34]. This example offers a prime illustration of how a careful theoretical treatment can definitively, and conclusively, reveal the intricate detail of physical processes which evade other more applied research approaches.

It is quite remarkable, given the physical importance of such flows, that apparently no analogous investigations have, to this point, been undertaken for internal wave motion. Of course, there has been substantial progress in the mathematical analysis of different aspects of internal wave motion in past years, particularly for nonlinear waves (cf. [2, 11, 9, 10, 13, 14, 15], and the references therein). The aim of this article is to investigate the fluid motion induced by internal water waves, coupled with surface waves, in the setting of two irrotational fluid layers, in the process achieving a detailed description of the underlying wave-field kinematics. It is assumed in this article that waves are periodic, travelling and linear, and furthermore that the coupled waves possess uniform wavelengths and frequency. Although they arise from a linearisation of the governing equations, the dynamical

systems which prescribe the fluid motion are themselves nonlinear, and so an intricate phase-plane analysis is required in order to comprehensively describe qualitative properties of the underlying fluid motion. Phase-plane approaches have previously proven successful in revealing the underlying flow-structure of surface water waves (cf. [7, 12, 16, 17, 22, 23]. Although these previous investigations are relevant to our description of fluid motion in the lower layer, the description of fluid motion in the upper layer requires a novel formulation and entails a new approach. In return, the flow patterns revealed in the upper fluid layer are particularly fascinating: phase-plane analysis exposes, and documents, a structure to the system that would otherwise be difficult to elucidate. For instance, phase-plane analysis furnishes us with an elegant and explicit visualisation of the transition process from in-phase, to out-of-phase, internal–surface wave coupling.

Along with an Eulerian characterisation of the wave-field kinematics for coupled internal and surface water waves, we pursue a Lagrangian description of fluid particle motion, in the process revealing some complex, and surprising, fluid particle trajectories. It has commonly been assumed (cf. [1]) that fluid particles undertake an orbital motion, which is greatest at the pycnocline: we establish that this is not always the case. We prove that no fluid particle fulfils closed trajectories in either of the fluid layers: indeed, every fluid particle undergoes a forward drift. The uniformity of this result is quite surprising given the range of possible motions exhibited by the various fluid particles. Furthermore, we establish monotonicity properties for the forward drift for a wide-range of possible physical scenarios. Regarding particle drift, it bears remarking that the Stokes' drift phenomenon (whereby fluid particles experience a mean net drift velocity in the direction of wave motion) is intrinsically nonlinear (cf. [26, 44]): the existence of a forward drift induced by linear internal waves for all fluid particles is apparently new.

1.1 Outline of article

The outline of this paper is as follows. In Section 2 the physical problem is introduced, and in Section 2.1 the equations of motion, together with boundary conditions, are systematically linearised in both fluid layers by way of suitable nondimensionalisation and scaling procedures. Adopting the standard *Ansatz* for linear travelling water waves, in Section 3 the governing equations are solved for coupled surface and internal waves with uniform wavelengths k and frequencies ω (equivalently, wavespeeds $c = \omega/k$). By considering compatibility conditions at both the internal and surface interfaces, dispersion relations are derived in the form of quadratic equations for c^2 or, alternatively, the nondimensional 'amplitude parameter' $A = g/kc^2$.

Dispersion relations for small-amplitude waves detail how the speed of the wave c propagating on an interface varies with respect to certain parameters, such as: the mean-depth of the fluid layers, the wavelength and, in the setting of internal waves, factors relating to the fluid stratification and the ratio of the magnitude of the internal/surface wave amplitudes. While the dispersion relation for the wavespeed in terms of c^2 is classical (cf. [31, 41]), its reformulation in terms of the nondimensional parameter A appears to offer a new insight into coupled wave motion. In particular, we show that there exists two possible solutions for A, which in turn represent two qualitatively distinct physical scenarios: for one solution the wave-crests of the internal wave coincides with the wave-crests of the surface wave (*in-phase* coupling), while for the other solution wave-crests of the internal wave coincide with wave-troughs of the surface wave (*out-of-phase* coupling). These relations are analysed and discussed in some detail in Section 3.3.

In Section 4 we analyse the dynamical systems which prescribe the underlying fluid motion for coupled surface and internal waves in the lower, and upper, fluid layers separately. Although they arise from a linearisation of the governing equations, the resulting dynamical systems themselves comprise nonlinear ordinary differential equations, and so a phase-plane analysis is employed in order to comprehensively ascertain qualitative features of the underlying fluid motion. Motion in the lower fluid layer is qualitatively similar to that induced by a linear surface wave propagating on a single fluid layer, however motion in the upper layer is significantly more convoluted and involved. It turns out that the dynamical system determining fluid motion in the upper layer generates three qualitatively different fluid motions, depending on whether the wave amplitude parameter A takes the values $A < 1$, $A = 1$, and $A > 1$, respectively. Accordingly, each case is treated separately.

Finally, in Section 5 the velocity field is subjected to a Lagrangian analysis which reveals that fluid particle trajectories are not closed, in general, for coupled internal and surface waves: each particle experiences a forward drift. We establish the monotonicity of particle drifts in the lower fluid layer, with partial monotonicity results presented for the upper layer. A complete qualitative description of particle paths in both fluid layers is obtained, with results in the upper layer being again contingent on the value of A. Fluid particle motion in the upper layer exhibits some complex and surprising characteristics.

2 Governing equations

We consider the two-dimensional motion of a stratified fluid, denoting horizontal and vertical coordinates by x and y, respectively. The fluid is assumed inviscid and incompressible, with an external restoration force due to gravity.

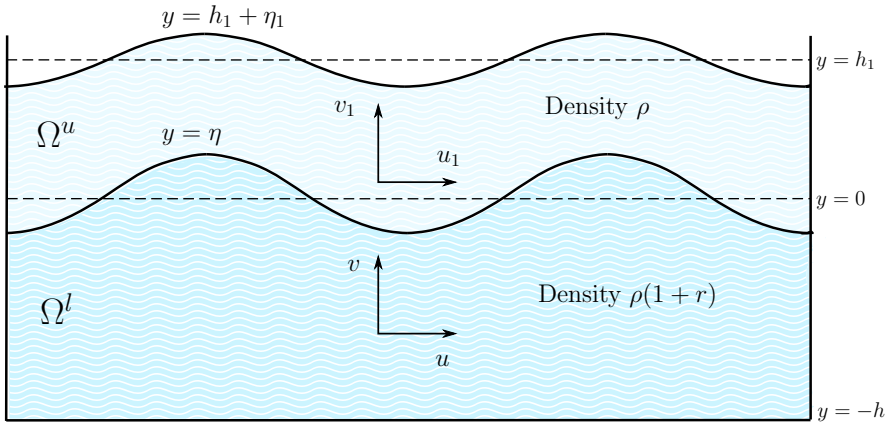


Figure 1: Schematic of the coupled surface-internal water wave problem.

The physical regime consists of two vertically stratified fluid layers of differing (but constant) densities separated by a sharp internal interface denoted by $y = \eta(x, t)$, which fluctuates about the mean water level $y = 0$: hence $\int_{\mathbb{R}} \eta(x, t)dx = 0$. The lower-fluid layer, which we denote by Ω^l, lies in the region $-h < y < \eta(x, t)$, where $y = -h$ is the location of the impermeable flat bed, and the velocity field is expressed as (u, v). The upper-fluid layer, denoted by Ω^u, lies in the region $\eta(x, t) \leq y \leq h_1 + \eta_1(x, t)$, where the *a priori* unknown free-surface boundary η_1 represents fluctuations around the undisturbed surface water level $y = h_1$, that is $\int_{\mathbb{R}} \eta_1(x, t)dx = 0$. The velocity field in the upper layer Ω^u is denoted (u_1, v_1). Here $h, h_1 > 0$ are physical constants which determine the mean-depths of the lower, and upper, layers respectively. We assume that η and η_1 are such that $\max|\eta(x, t)| < h$, and $\max|\eta(x, t)| + \max|\eta_1(x, t)| < h_1$, which precludes any intersection of the surface and internal wave interfaces. We assume stable stratification, with the upper layer being less dense than the lower layer, in which case we denote the density of the upper layer by ρ and the lower layer by $(1 + r)\rho$, where $r > 0$ is constant. In practice $r \ll 1$: for instance, in an oceanographical context, the value $r = \mathcal{O}(10^{-3})$ may be taken as reasonable [10, 30].

The equations of motion for an inviscid and incompressible fluid are the Euler equation, which is expressed in the lower layer Ω^l by The equations of

motion for an inviscid and incompressible fluid are the Euler equation, which is expressed in the lower layer Ω^l by

$$\begin{aligned} u_t + uu_x + vu_y &= -\frac{P_x}{\rho(1+r)}, \\ v_t + uv_x + vv_y &= -\frac{P_y}{\rho(1+r)} - g, \end{aligned} \tag{1a}$$

together with the equation of continuity

$$u_x + v_y = 0. \tag{1b}$$

The scalar function $P(x, y, t)$ represents the internal fluid pressure, and g denotes the gravitational acceleration constant. In the upper-fluid layer Ω^u

$$\begin{aligned} u_{1,t} + u_1 u_{1,x} + v_1 u_{1,y} &= -\frac{P_{1,x}}{\rho}, \\ v_{1,t} + u_1 v_{1,x} + v_1 v_{1,y} &= -\frac{P_{1,y}}{\rho} - g, \end{aligned} \tag{2a}$$

$$u_{1,x} + v_{1,y} = 0. \tag{2b}$$

The kinematic boundary condition in the lower layer Ω^l at the impermeable flat bed is

$$v = 0 \qquad \text{on } y = -h. \tag{3a}$$

The dynamic and kinematic boundary conditions at the internal interface take the form

$$P = P_1 \qquad \text{at } y = \eta(x,t). \tag{3b}$$

$$v_1 = \eta_t + u_1\eta_x \qquad \text{on } y = \eta(x,t), \tag{3c}$$

$$v = \eta_t + u\eta_x \qquad \text{on } y = \eta(x,t), \tag{3d}$$

The dynamic boundary condition (3b) ensures that the pressure is always continuous throughout a fluid. The kinematic boundary conditions (3c) and (3d) ensure that the the normal components of the respective velocity fields match, and are continuous, at the interface. For inviscid fluid motion this need not be true for the tangential velocity components. Finally, at the free-surface, the governing equations (2) in the upper layer Ω^u have the associated dynamic and kinematic boundary conditions

$$P_1 = P_{atm} \qquad \text{on } y = h_1 + \eta_1(x,t), \tag{3e}$$

$$v_1 = \eta_{1,t} + u_1\eta_{1,x} \qquad \text{on } y = h_1 + \eta_1(x,t). \tag{3f}$$

The fluid is assumed to be irrotational in each fluid layer separately which, in two-dimensions, corresponds to

$$u_y = v_x, \qquad u_{1,y} = v_{1,x}. \tag{4}$$

Accordingly, define the velocity potentials $\varphi(x, y, t)$ in the lower-fluid layer Ω^l, and $\varphi_1(x, y, t)$ in the upper-fluid layer Ω^u, by

$$\nabla\varphi = (u, v), \qquad \nabla\varphi_1 = (u_1, v_1). \tag{5}$$

It follows from the definition (5), coupled with the incompressibility equations (1b) and (2b), that the velocity potentials are harmonic functions:

$$\Delta\varphi = \Delta\varphi_1 = 0. \tag{6}$$

2.1 Linearisation procedure

The governing equations, and boundary conditions, can be linearised by invoking nondimensionalisation and scaling procedures as follows. Let λ be a characteristic wavelength for the water waves being considered, and let $\mathfrak{h}$ be a characteristic depth scale such that $h, h_1 \sim \mathcal{O}(\mathfrak{h})$. Let a be a characteristic amplitude of the internal wave, with a_1 a characteristic amplitude for the surface wave. We define nondimensional variables and functions by mapping

$$\begin{aligned} &x \mapsto \lambda x,\ y \mapsto \mathfrak{h} y,\ t \mapsto \frac{\lambda}{\sqrt{g\mathfrak{h}}} t,\ \eta \mapsto a\eta,\ \eta_1 \mapsto a_1\eta_1, \\ &(u, v) \mapsto \left(u\sqrt{g\mathfrak{h}}, v\frac{\mathfrak{h}\sqrt{g\mathfrak{h}}}{\lambda}\right),\ (u_1, v_1) \mapsto \left(u_1\sqrt{g\mathfrak{h}}, v_1\frac{\mathfrak{h}\sqrt{g\mathfrak{h}}}{\lambda}\right), \end{aligned} \tag{7}$$

where for example we replace x by λx, with x now being a nondimensionalised variable, thus avoiding new notation. We express the pressure in terms of the new nondimensional variables by

$$\begin{cases} P = P_{atm} + g\rho\mathfrak{h}\tilde{h}_1 - g\rho(1+r)\mathfrak{h}y + g\rho(1+r)\mathfrak{h}p, & -\tilde{h} < y < \epsilon\eta, \\ P_1 = P_{atm} + g\rho\mathfrak{h}(\tilde{h}_1 - y) + g\rho\mathfrak{h}p_1, & \epsilon\eta \le y \le \tilde{h}_1 + \epsilon_1\eta_1, \end{cases}$$

where the nondimensional pressure functions p, p_1 measure the deviation from the hydrostatic pressure distribution. Here $\epsilon = a/\mathfrak{h}$, $\epsilon_1 = a_1/\mathfrak{h}$ are nondimensional parameters which measure the magnitude of the wave amplitudes relative to the characteristic vertical depth scale, while $\tilde{h} = h/\mathfrak{h}$, $\tilde{h}_1 = h_1/\mathfrak{h}$

are nondimensional parameters such that $\tilde{h}, \tilde{h}_1 \sim \mathcal{O}(1)$. The governing equations (1a), (1b) get transformed to

$$\begin{cases} u_t + uu_x + vu_y = -p_x, \\ \delta^2 (v_t + uv_x + vv_y) = -p_y, \\ u_x + v_y = 0, \end{cases} \tag{8a}$$

in the domain $-\tilde{h} < y < \epsilon\eta$; the governing equations (2a) and (2b) get transformed to

$$\begin{cases} u_{1,t} + u_1 u_{1,x} + v_1 u_{1,y} = -p_{1,x}, \\ \delta^2 (v_{1,t} + u_1 v_{1,x} + v_1 v_{1,y}) = -p_{1,y}, \\ u_{1,x} + v_{1,y} = 0, \end{cases} \tag{8b}$$

in the domain $\epsilon\eta \leq y \leq \tilde{h}_1 + \epsilon_1\eta_1$; while the boundary conditions (3a)–(3f) become

$$\begin{cases} v = 0 & \text{on } y = -\tilde{h}, \\ v = \epsilon (\eta_t + u\eta_x) & \text{on } y = \epsilon\eta, \\ v_1 = \epsilon (\eta_t + u_1\eta_x) & \text{on } y = \epsilon\eta, \\ p_1 = (1+r)p - r\epsilon\eta & \text{at } y = \epsilon\eta, \\ v_1 = \epsilon_1 (\eta_{1,t} + u_1\eta_{1,x}) & \text{on } y = \tilde{h}_1 + \epsilon_1\eta_1. \\ p_1 = \epsilon_1\eta_1 & \text{on } y = \tilde{h}_1 + \epsilon_1\eta_1. \end{cases} \tag{8c}$$

Here $\delta = \mathfrak{h}/\lambda$ is a nondimensional 'shallowness' parameter which measures the magnitude of the characteristic vertical depth scale relative to the wavelength. From (8c) it is clear that v, v_1, p, p_1 are essentially proportional to ϵ when evaluated on $y = \epsilon\eta$, while v_1, p_1 are proportional to ϵ_1 when evaluated on $y = \tilde{h} + \epsilon_1\eta_1$. With this in mind, we scale the nondimensional variables as follows:

$$(u, v) \mapsto \epsilon(u, v), \quad p \mapsto \epsilon p, \quad (u_1, v_1) \mapsto \epsilon_1(u_1, v_1), \quad p_1 \mapsto \epsilon_1 p_1, \tag{9}$$

avoiding again the introduction of new variables. Now problem (8) becomes

$$\begin{cases} u_t + \epsilon (uu_x + vu_y) = -p_x, \\ \delta^2 (v_t + \epsilon (uv_x + vv_y)) = -p_y, \\ u_x + v_y = 0, \end{cases} \tag{10a}$$

in the domain $-\tilde{h} < y < \epsilon\eta$;

$$\begin{cases} u_{1,t} + \epsilon_1 (u_1 u_{1,x} + v_1 u_{1,y}) = -p_{1,x}, \\ \delta^2 (v_{1,t} + \epsilon_1 (u_1 v_{1,x} + v_1 v_{1,y})) = -p_{1,y}, \\ u_{1,x} + v_{1,y} = 0, \end{cases} \tag{10b}$$

in the domain $\epsilon\eta \leq y \leq \tilde{h}_1 + \epsilon_1\eta_1$;

$$\begin{cases} v = 0 & \text{on } y = -\tilde{h}, \\ v = \eta_t + \epsilon u \eta_x & \text{on } y = \epsilon\eta, \\ v_1 = \mathfrak{a}\left(\eta_t + \epsilon_1 u_1 \eta_x\right) & \text{on } y = \epsilon\eta, \\ p_1 = (1+r)\mathfrak{a}p - r\mathfrak{a}\eta & \text{at } y = \epsilon\eta, \\ v_1 = \eta_{1,t} + \epsilon_1 u_1 \eta_{1,x} & \text{on } y = \tilde{h}_1 + \epsilon_1\eta_1. \\ p_1 = \eta_1 & \text{on } y = \tilde{h}_1 + \epsilon_1\eta_1. \end{cases} \tag{10c}$$

Here $\mathfrak{a} = a/a_1$. The linearised problem is obtained by letting $\epsilon, \epsilon_1 \to 0$ in (10): let us assume that the limiting procedure is such that $\mathfrak{a}$ remains finite, if not we simply re-express the relevant equations in (10c) in terms of the inverse of $\mathfrak{a}$. The resulting nondimensionalised, scaled and linearised governing and boundary equations for the two-dimensional motion of coupled internal and surface water waves are then given by:

$$\begin{cases} u_t = -p_x, \quad \delta^2 v_t = -p_y, \\ u_x + v_y = 0, \end{cases} \qquad \text{in } -\tilde{h} < y < 0, \tag{11a}$$

$$\begin{cases} u_{1,t} = -p_{1,x}, \quad \delta^2 v_{1,t} = -p_{1,y}, \\ u_{1,x} + v_{1,y} = 0, \end{cases} \qquad \text{in } 0 \leq y \leq \tilde{h}_1, \tag{11b}$$

$$\begin{cases} v = 0 & \text{on } y = -\tilde{h}, \\ v = \eta_t, \quad v_1 = \mathfrak{a}\eta_t, \quad p_1 = (1+r)\mathfrak{a}p - r\mathfrak{a}\eta & \text{on } y = 0, \\ v_1 = \eta_{1,t}, \quad p_1 = \eta_1 & \text{on } y = \tilde{h}_1. \end{cases} \tag{11c}$$

Reversing the scaling (9) and nondimensionalisation (7) transformations we obtain the linearised governing equations in terms of the physical variables:

$$\begin{cases} u_t = -\dfrac{P_x}{\rho(1+r)}; \quad v_t = -\dfrac{P_y}{\rho(1+r)}, & \text{(12a)} \\ u_x + v_y = 0 \qquad\qquad \text{in } -h < y < 0, & \text{(12b)} \end{cases}$$

$$\begin{cases} u_{1,t} = -\dfrac{P_{1,x}}{\rho}; \quad v_{1,t} = -\dfrac{P_{1,y}}{\rho} - g, & \text{(13a)} \\ u_{1,x} + v_{1,y} = 0 \qquad\qquad \text{in } 0 \leq y \leq h_1, & \text{(13b)} \end{cases}$$

$$\begin{cases} v = 0 & \text{on } y = -h, \quad (14a) \\ v = \eta_t; \quad v_1 = \eta_t; \quad P_1 = P - g\rho r\eta & \text{on } y = 0, \quad (14b) \\ v_1 = \eta_{1,t}; \quad P_1 = P_{atm} + g\rho\eta_1 & \text{on } y = h_1. \quad (14c) \end{cases}$$

We note that the linearisation process eliminates all product terms in the governing equations (1), (2), and the boundary conditions (3), as expected. Importantly, the boundary conditions are also now evaluated at the constant mean levels $y = 0, h_1$, as opposed to on the unknown interfaces: contrast (3) with (14).

3 Travelling wave solutions

In the following we seek solutions that are periodic travelling waves. For travelling waves there is a functional dependence on the x and t variables of the form $kx-\omega t$, where ω is the wave frequency, $k = 2\pi/\lambda$ is the wavenumber, and $c = \omega/k$ is the wave phasespeed. To construct solutions of the linearised governing equations (**??**)–(**??**), in terms of the velocity potentials defined in (5), the following Ansatz for linear travelling wave solutions is invoked:

$$\eta(x,t) = a\cos(kx - \omega t), \quad (15a)$$
$$\eta_1(x,t) = a_1\cos(kx - \omega t), \quad (15b)$$

where a_1 and a are the amplitudes of the free-surface, and interface, respectively. The ansatz (15) assumes that waves coupled at the free-surface and interface have identical wavelengths and periods: how this reconciles with physical observations will be discussed in Section 3.3.2 below. Unless otherwise stated, in the following we assume that $a, a_1 \neq 0$, thereby implying a non-trivial coupling of wave motions at the free-surface and the interface. Limiting processes which result in either wave amplitude vanishing (and the associated 'one free-interface' models) are discussed in the context of dispersion relations in Section 3.3.3. We remark that the physical set-up in Figure 1 represents waves where the crests (and troughs) of the surface and internal interfaces coincide, which corresponds to the ratio $a/a_1 > 0$ in (15). The ansatz (15) permits an alternative configuration, whereby the crests (respectively, troughs) of the surface wave coincides with the troughs (respectively, crests) of the internal wave. This scenario arises when $a/a_1 < 0$, and is represented in the following schematic:

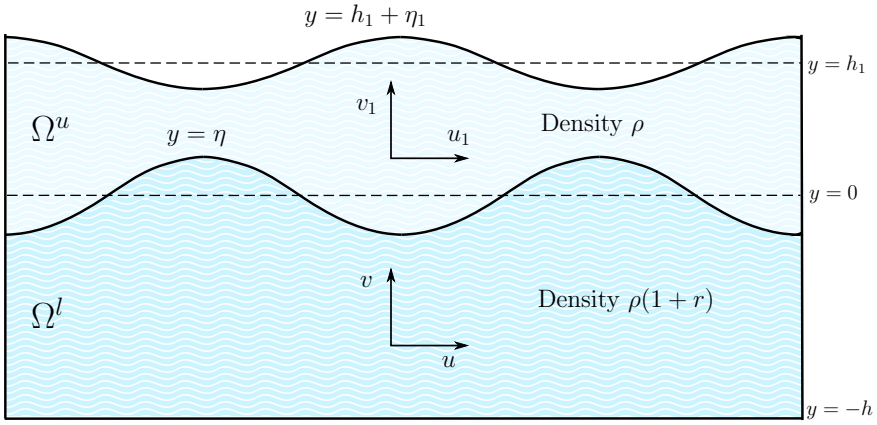


Figure 2: Coupled surface-internal water waves for $a/a_1 < 0$.

In the following, we refer to the coupled waves represented in Figure 1, with $a/a_1 > 0$, as being 'in-phase', whereas the coupled waves represented in Figure 2, with $a/a_1 < 0$, will be referred to as being 'out-of-phase'. We note that $|a| + |a_1| < h_1$ must hold for out-of-phase waves. In relation (36) we establish, through analysis of dispersion relations, that there exists precisely one set of coupled wave solutions which are in-phase, and one set which are out-of-phase, for a given fixed wavelength (or, alternatively, fixed frequency).

3.1 Velocity potential

3.1.1 Lower-fluid layer

In Ω^l the velocity potential φ must be harmonic (6), and should satisfy the boundary conditions given by (14a) and the first equation in (14b), re-expressed using the definition (5) and substituting the ansatz (15a). Hence, φ must solve the Neumann boundary value problem

$$\begin{aligned} \Delta\varphi &= 0 && \text{for } -h < y < 0, \\ \varphi_y &= akc\sin(kx - \omega t) && \text{on } y = 0, \\ \varphi_y &= 0 && \text{on } y = -h. \end{aligned}$$

This has the solution

$$\varphi(x, y, t) = ac\frac{\cosh k(y + h)}{\sinh kh}\sin(kx - \omega t) \quad \text{in } -h < y < 0. \tag{17}$$

3.1.2 Upper-fluid layer

In Ω^u the velocity potential φ_1 must be harmonic (6) and must additionally solve the boundary conditions given by the second equation in (14b) and the first equation in (14c), re-expressed once more using (5) and ansatz (15). Hence, φ_1 must solve the Neumann boundary value problem

$$\begin{aligned} \Delta\varphi_1 &= 0 && \text{for } 0 < y < h_1, \\ \varphi_{1,y} &= a_1 kc \sin(kx - \omega t) && \text{on } y = h_1, \\ \varphi_{1,y} &= akc \sin(kx - \omega t) && \text{on } y = 0. \end{aligned}$$

This has the solution

$$\varphi_1(x, y, t) = a_1 c \sin(kx - \omega t) \left\{ \sinh k(y - h_1) + A \cosh k(y - h_1) \right\} \quad \text{in } 0 < y < h_1, \tag{19}$$

where the nondimensional parameter A is given by

$$A = \left(1 - \frac{a}{a_1} \operatorname{sech}(kh_1) \right) \coth(kh_1). \tag{20}$$

The value of A is itself determined by two nondimensional parameters, namely: the ratio of wave amplitudes a/a_1; and the shallowness parameter $kh_1 = 2\pi \cdot h_1/\lambda$. Note that the limiting case $a_1 \to 0$ (no surface wave) in the upper fluid layer corresponds to the classical 'rigid lid' model of internal wave motion, with velocity potential

$$\varphi_1(x, y, t) = -ac \frac{\cosh k(y - h_1)}{\sinh(kh_1)} \sin(kx - \omega t) \text{ in } 0 < y < h_1. \tag{21}$$

3.1.3 Continuity of normal velocities at internal interface

At the interface we have an additional constraint requiring the continuity of normal velocities, as prescribed by the first two equations in (14b), which can be expressed as

$$\varphi_{1,y} = \varphi_y \text{ on } y = 0. \tag{22}$$

Substituting (17) and (19) leads to

$$\frac{a}{a_1} = \cosh kh_1 - A \sinh kh_1, \tag{23}$$

an identity which is satisfied as a consequence of the definition of A in (20).

3.2 Pressure distribution

3.2.1 Lower-fluid layer

Substituting solution (17) into the linearised Euler equation (12a) leads to equations which can be solved to get the pressure distribution in Ω^l as:

$$\frac{P}{\rho} = \tilde{P} + akc^2(1+r)\frac{\cos(kx-\omega t)}{\sinh kh}\cosh k(y+h) - gy(1+r), \tag{24}$$

for $-h < y < 0$, where $\tilde{P}$ is a constant.

3.2.2 Upper-fluid layer

Similarly, substituting (19) into (13a) gives the pressure distribution in Ω^u as:

$$\frac{P_1}{\rho} = \tilde{P}_1 + a_1 c\cos(kx-\omega t)\left[\omega\sinh k(y-h_1) + A\omega\cosh k(y-h_1)\right] \tag{25}$$
$$-g(y-h_1),$$

in $0 < y < h_1$, where $\tilde{P}_1$ is a constant.

3.2.3 Pressure-matching at the free-surface

The pressure distribution (25) must satisfy the dynamic boundary condition at the linearised free-surface $y = h_1$ given by the second equation in (14c), namely: $P_1 = P_{atm} + g\rho\eta_1$ on $y = h_1$. Setting $y = h_1$ in (25), and using (15b), we have

$$\rho a_1 c\cos(kx-\omega t)A\omega + \rho\tilde{P}_1 = P_{atm} + g\rho a_1\cos(kx-\omega t),$$

which can only hold if $\tilde{P}_1 = P_{atm}/\rho$ and if the coefficients of the cosine function sum to zero resulting (using (20)) in the condition:

$$c^2 = \frac{g}{k}\frac{1}{A} = \frac{g}{k}\tanh(kh_1)\left(1 - \frac{a}{a_1}\mathrm{sech}\,(kh_1)\right)^{-1}. \tag{26}$$

This is the dispersion relation at the free-surface. However it is important to note that this is not a dispersion relation for the surface wave alone: there is an intrinsic coupling between surface and internal wave parameters involved in the ratio a/a_1. An immediate consequence of (26) is that the parameter A must be positive, which confers a bound on the internal wave amplitude for in-phase waves, namely:

$$a < a_1\cosh(kh_1), \qquad \text{when } a/a_1 > 0.$$

3.2.4 Pressure-matching at the internal interface

The pressure distributions (24) and (25) must satisfy the dynamic boundary condition given by the third condition in (14b) at the linearised internal interface $y = 0$, that is: $P_1 = P - g\rho r\eta$ on $y = 0$. This condition ensures the continuity of pressure between the upper and lower-fluid layers. Examining (25) and (24) we conclude that this condition can hold only if $\tilde{P} = \tilde{P}_1 + gh_1 = P_{atm}/\rho + gh_1$, and additionally

$$a_1 kc\,[-c\sinh kh_1 + Ac\cosh kh_1] = ac(1+r)\frac{kc}{\tanh kh} - gar. \tag{27}$$

This is the dispersion relation at the interface however, as remarked for equation (26), this is not the dispersion relation for the interface alone. This relation features coupling between surface and internal waves by way of terms involving the ratio of wave amplitudes.

3.3 Dispersion relations for the coupled waves

A dispersion relation is a formula which specifies the linear wavespeed c in terms of various physical parameters. It is so-called since if the wavespeed c varies with respect to some parameter then the waves are dispersive: waves corresponding to different parameter values will travel at different speeds. Assuming we know (either by measurement, or prescription) the mean depths h, h_1 of the fluid layers, equations (26) and (27) features three unknown parameters, namely the wavenumber $k = 2\pi/\lambda$, the wavespeed $c = \omega/k$ (or, alternatively, the frequency ω), and the ratio of wave amplitudes a/a_1. Using (23) we can re-express (26) as

$$\frac{a}{a_1} = \cosh(kh_1) - \frac{g}{kc^2}\sinh(kh_1), \tag{28}$$

and (27) as a quadratic for c as:

$$\left[\operatorname{sech} kh_1 - \frac{a}{a_1}\left\{1 + (1+r)\frac{\tanh kh_1}{\tanh kh}\right\}\right]\frac{kc^2}{g} + r\frac{a}{a_1}\tanh kh_1 = 0. \tag{29}$$

These identities clearly express how the wavespeed c is contingent on the ratio of wave-amplitudes, a/a_1, and *vice-versa*. Together, equations (28) and (29) constitute a system of dispersion relations prescribing the wavespeed c of coupled internal and surface waves, and the ratio a/a_1 of associated wave-amplitudes, in terms of the wavenumber k. A useful initial approach when examining dispersion relations is adopted by assuming that k is a 'known'

parameter, in the sense that the wavelength can either be prescribed, or determined by measurement: in this scenario we consider the wavenumber k to be fixed.

Substituting (28) into (29) leads to the classical dispersion relation [31, 41] for the wavespeed:

$$\left\{1+\frac{1+r}{\tanh kh_1\tanh kh}\right\}\frac{k^2c^4}{g^2}-(1+r)\left\{\frac{1}{\tanh kh_1}+\frac{1}{\tanh kh}\right\}\frac{kc^2}{g}+r=0. \tag{30}$$

The nondimensional parameter A plays a key role in our examination of the underlying fluid motion induced by coupled waves in Section 4, and we observe that it arises naturally in (30) by way of the term $kc^2/g = 1/A$. It is therefore propitious to reformulate relation (30) as

$$rA^2-(1+r)\left\{\frac{1}{\tanh kh_1}+\frac{1}{\tanh kh}\right\}A+\left\{1+\frac{(1+r)}{\tanh kh_1\tanh kh}\right\}=0. \tag{31}$$

This constitutes a dispersion relation for the ratio of wave amplitudes since, given solutions of (31), the ratio of the corresponding wave-amplitudes a/a_1 can be established directly from (23) (in terms of k). The roots, A_1 and A_2, of the quadratic equation (31) are real, since the discriminant

$$\Delta=(1+r)^2\left\{\frac{1}{\tanh kh_1}-\frac{1}{\tanh kh}\right\}^2+4r\left\{\frac{1}{\tanh kh_1\tanh kh}-1\right\} +\frac{4}{\tanh kh_1\tanh kh}>0. \tag{32}$$

Examining the coefficients of (31), we further conclude that both roots are positive, $A_1, A_2 > 0$ (which is consistent with (26)), while relation (32) implies that they are unequal. Indeed, direct computation gives

$$A_{1,2}=\frac{1}{2r}\left[(1+r)\left\{\frac{1}{\tanh kh_1}+\frac{1}{\tanh kh}\right\}\mp\sqrt{\Delta}\right]. \tag{33}$$

Let us take $A_2 > A_1$. Denoting (31) as $\mathcal{P}(A) = 0$, it follows by calculation that

$$\mathcal{P}\left(\frac{1}{\tanh kh_1}\right)=1-\frac{1}{\tanh^2 kh_1}<0,\qquad \mathcal{P}\left(\frac{1}{\tanh kh}\right)=1-\frac{1}{\tanh^2 kh_1}<0,$$

giving the relations (which we note are independent of the relative densities):

$$A_1<\frac{1}{\tanh kh_1}<A_2,\qquad A_1<\frac{1}{\tanh kh}<A_2. \tag{34}$$

Furthermore if, for instance, $r < 1$, the quantity

$$\mathcal{P}\left(\frac{1}{\tanh kh_1}+\frac{1}{\tanh kh_1}\right)=1-\frac{1}{\tanh^2 kh_1}-\frac{1}{\tanh^2 kh}+\frac{r-1}{\tanh kh\tanh kh_1},$$

is negative. Typically $r \ll 1$ in an oceanographical context, with $r=\mathcal{O}(10^{-3})$ constituting a reasonable value [10, 30]. In this case

$$A_2 > \frac{1}{\tanh kh_1}+\frac{1}{\tanh kh}. \tag{35}$$

It can be concluded from (23) that

$$\frac{a}{a_1}<0 \Longleftrightarrow A > \frac{1}{\tanh kh_1},$$

and together with (34) we infer that

$$\frac{a}{a_1}>0 \text{ for } A=A_1, \qquad \frac{a}{a_1}<0 \text{ for } A=A_2. \tag{36}$$

Coupled wave motions at the interface and free-surface are in-phase for solutions corresponding to the root $A = A_1$, and out-of-phase for $A = A_2$.

Remark 1 In relation to the phase-portrait analysis that we undertake in Section 4.2, when examining fluid motion in the upper-fluid layer, we note that a consequence of (34) is that one of the roots of (31), A_2, is *always* greater than one. In general, A_1 may be greater than, less than, or equal to one, depending on the physical parameters of the wave problem we consider.

Remark 2 A discontinuity in tangential fluid velocities always occurs at the internal interface. This can be seen by comparing φ_x and $\varphi_{1,x}$ (which correspond to the linearised tangential velocities in the respective layers) at $y = 0$. By (17) and (19), these match only if $a\coth kh = a_1\{-\sin kh_1 + A\cosh kh_1\}$, and, using (27), this holds only if $kc^2/g = 1/A = \tanh kh$. Relation (34) shows that this equality can never hold. Hence, although the fluid is irrotational in each fluid layer separately, there is a vortex sheet located at the internal interface. In practice, viscosity (which has been neglected in this model) acts to blur the sheet into a vortex film.

3.3.1 Wavespeed solutions

The roots of (30), the dispersion relation for the wavespeeds, can be determined from (33) using $c^2 = g/kA$ to get

$$c_{1,2}^2=\frac{g}{k}\frac{\tanh kh_1\tanh kh}{2(1+r)+2\tanh kh_1\tanh kh}\left[(1+r)\left\{\frac{1}{\tanh kh_1}+\frac{1}{\tanh kh}\right\}\pm\sqrt{\Delta}\right]. \tag{37}$$

Each root c_i^2 in (37) represents a given wavespeed, with the choice of sign $+c_i$ (or $-c_i$) corresponding to right-moving (or left-moving) coupled waves respectively. It follows from (37) that $c_1 > c_2 > 0$, which accords with the root c_i being associated with A_i. The nomenclature *barotropic*, and *baroclinic*, has been applied to the wavespeeds c_1, and c_2, respectively, cf. [41]. Using (26), relations (34) and (35) lead to

$$c_2 < \sqrt{\frac{g}{k}\frac{\tanh kh \tanh kh_1}{\tanh kh + \tanh kh_1}}, \quad c_1 > \max\left\{\sqrt{\frac{g}{k}\tanh kh_1}, \sqrt{\frac{g}{k}\tanh kh_1}\right\}.$$

3.3.2 Physical interpretations

Typically, it is observed that internal waves are much slower than surface waves, with significantly greater amplitudes. This is due to the restoring force at the internal interface being substantially less than at the free surface. Internal waves in the ocean can have periods ranging from tens of minutes to several hours, with wavelengths ranging from hundreds of meters to tens of kilometres, and their height can often exceed 50m (cf. [18, 20, 32, 41]). In contrast, for ocean surface gravity waves the period ranges from 1 to 25 seconds, with ocean swell having a typical wavelength that is greater than 260m (up to a maximum of approximately 900m) with a period larger than 13s (up to a maximum of 24s) (cf. [42]).

We expect these properties to be reflected in the solutions of the linear dispersion relations above. In particular, given the same wavelength, the speed of propagation should be much smaller for internal wave solutions than for surface waves. However, as stated previously, the dispersion relations (28) and (29) govern the motion of coupled surface and internal waves. Hence, given a solution corresponding to a specific wavelength and wavespeed, we cannot take it to apply to either the surface, or internal, wave in isolation. In the linear framework, wherever there is a surface wave travelling with a particular wavelength and wavespeed there will be a corresponding internal wave solution, and *vice versa*.

A resolution between this mathematical formulation, and physical observations, can be achieved (for fixed wavelengths) if we establish that the amplitude of the internal wave a is more significant than that of the surface wave a_1 at slower wavespeeds. Indeed, the root corresponding to the slower wavespeed, c_2, pertains to out-of-phase waves and, from relation (26) (with k fixed), we can infer that wavespeeds are minimised as $a/a_1 \to -\infty$, and maximised as $a/a_1 \to 0$. Hence, the slowest waves are those where the internal wave amplitude is significantly larger than that of the surface wave. For in-phase waves, which corresponds to the faster c_1 root, relation

(26) implies that the wavespeed is minimised as $a/a_1 \to 0$, and maximised as $a/a_1 \to \cosh(kh_1)$. In this case the presence of internal wave motion increases the wavespeed of the coupled surface and internal waves.

Furthermore, considering variable wavelengths, based on physical observations we would expect the amplitude of (faster) surface waves to predominate in the coupled system for smaller wavelengths (larger k), while for longer wavelengths (smaller k) we expect the (slower) internal waves to prevail. Establishing the change in behaviour of the wave solutions (namely, the wavespeeds and amplitude ratios) with respect to the wavenumber is difficult to elucidate in general, but insight can be gained by examining the limiting cases $k \to \infty$, and $k \to 0$.

For sufficiently large k (such that $\tanh(kh_1), \tanh(kh) \approx 1$) (37) becomes

$$c_1^2 \approx \frac{g}{k}, \qquad c_2^2 \approx \frac{gr}{k(2+r)} = \frac{g}{k}\frac{\rho-\rho_1}{\rho+\rho_1}, \tag{38}$$

and so $c_2 \ll c_1$ for $r \ll 1$. By (33), $A_1 = 1$, $A_2 = (2+r)/r = (\rho-\rho_1)/(\rho+\rho_1)$ for large k. For the root $A_1 = 1$, (23) gives $a/a_1 = e^{-kh_1} \to 0$: the surface and internal waves are in-phase for the fast wavespeed solution, with the amplitude at the surface being far greater than that at the interface. For $A_2 = (2+r)/r$, inserting directly into (23) gives $a/a_1 = -e^{kh_1}/r + (1+r)e^{-kh_1}/r \to -e^{kh_1}/r$: the surface and internal waves are out-of-phase for the slow wavespeed solution, with the amplitude of the surface wave being negligible compared to the internal wave. For sufficiently large k the terms 'fast' and 'slow' are relative, as $c_{1,2} \to 0$ in the limiting case $k \to \infty$. Of course, when considering limiting procedures we must bear in mind that the linear framework applies only for $\epsilon = a/\lambda, \epsilon_1 = a_1/\lambda \ll 1$, and so $k \to \infty$ implies $a, a_1 \to \infty$: there is no wave motion.

For sufficiently small k (such that $\sinh(kh_1) \approx kh_1$, $\sinh(kh) \approx kh$, and $\cosh kh_1, \cosh kh \approx 1$) formula (37) becomes

$$c_{1,2}^2 = \frac{gh_1h}{2(1+r)}\left[(1+r)\left\{\frac{1}{h_1}+\frac{1}{h}\right\} \pm (1+r)\left\{\frac{1}{h_1}+\frac{1}{h}\right\} \mp \frac{2r}{h+h_1} + \mathcal{O}(r^3)\right],$$

that is (neglecting terms of order $\mathcal{O}(r^3)$):

$$c_1^2 = g(h_1+h) - \frac{rgh_1h}{(1+r)(h+h_1)}, \qquad c_2^2 = \frac{rgh_1h}{(1+r)(h+h_1)}. \tag{39}$$

In this physical regime relation (28) takes the form

$$\frac{a}{a_1} = 1 - \frac{gh_1}{c^2}. \tag{40}$$

Inserting the slower wavespeed from (39), c_2, into (40) gives

$$\frac{a}{a_1} = -\frac{1}{r} - \mathcal{H}\left(1 + \frac{1}{r}\right), \tag{41}$$

where the nondimensional parameter $\mathcal{H} = h_1/h$ gives the ratio of the mean-depth of the upper and lower layers. For small r, this relation implies that the surface and internal waves are out-of-phase, with the amplitude of the surface wave being negligible compared to the internal wave. Inserting the faster wavespeed in (39), c_1, in (40) gives

$$\frac{a}{a_1} = \frac{h(h+h_1) + rh^2}{(h+h_1)^2 + r(h_1^2 + hh_1 + h^2)} = \frac{(1+\mathcal{H}) + r}{(1+\mathcal{H})^2 + r(\mathcal{H}^2 + \mathcal{H} + 1)}, \tag{42}$$

and the surface wave amplitude is larger than the internal wave. Interestingly, both (41) and (42) feature the depth-ratio parameter $\mathcal{H}$.

Accordingly, investigations of the limiting cases above do suggest that the amplitude of the internal wave predominates that of the surface wave at slower wavespeeds, and for longer wavelengths whereas, converely, the amplitude of the surface wave prevails for faster wavespeeds, and shorter wavelengths, as prescribed by the dispersion relations (30), (31). Nevertheless, an ineluctable consequence of our deliberations is that short, fast waves must also exist at the internal interface, as do slow, long waves at the surface. Such waves seemingly constitute aberrations from the observed physical properties of surface and internal waves. However, these apparently anomalous wave solutions may be indiscernible in practice given their relatively small amplitudes: wave solutions are simply added together in the linear regime to which our considerations pertain, hence slow-surface/fast-internal waves may be dwarfed by their fast-surface/slow-interface counterparts, respectively.

Of course, the linear framework enforces a number of inherent limitations on the size of the wave: the linearisation procedure implemented in Section 2.1 confers *a priori* restrictions on the wave amplitudes given by $a/\lambda, a_1/\lambda \ll 1$, while the phase-plane analysis of the next section details further constraints due to the bounds (48), (54), (55) and (57). Evidently, a thorough understanding of large amplitude waves requires nonlinear analysis. Nevertheless, it is clear that a detailed analysis of the linear system is a first step towards gaining rich insight into a range of complex physical properties intrinsic to coupled surface and internal waves.

3.3.3 Dispersion relations — limiting cases

Remark 3 Letting $r \to 0$ simplifies the physical model, which now consists of one homogeneous fluid layer of mean-depth $h + h_1$. Taking $r \to 0$ in (37)

leads to $c_2 = 0$ and $c_1^2 = g\tanh(k\,[h+h_1])/k$: this is the classical dispersion relation for a surface wave over fluid of finite depth $h + h_1$.

Remark 4 Taking $r \to \infty$ in (37) gives $c_{1,2}^2 = g\tanh(kh)/k, g\tanh(kh_1)/k$, with the ordering determined by whichever of h, h_1 is larger. These are the dispersion relations for surface waves propagating on a fluid of depth h, respectively h_1. Physically, this limit corresponds to the lower-layer being infinitely denser than the upper-layer which (as can be inferred from the dispersion relations) essentially results in the decoupling of wave motions in both layers. The extreme disparity in densities renders the wave motion in either layer effectively independent of the other.

Remark 5 Setting $a = 0$ gives $A = \coth kh_1$ and $c^2 = g\tanh kh_1/k$. This is the classical dispersion relation for wave propagation on the surface of a single fluid layer of depth h_1 over a 'flat bed'. In this case the undisturbed internal interface constitutes a flat boundary. This value of A plays an important role in the phase-plane analysis of the next section.

Remark 6 The 'rigid-lid' model describes wave motion at the interface separating two fluid layers which are bounded above, and below, by horizontal rigid walls. If the mean thickness of the upper-layer is h_1, and the lower-layer h, the dispersion relationship takes the form [31]

$$c^2 = \frac{g}{k}\frac{\rho^{lower} - \rho^{upper}}{\rho^{lower}\,\coth(kh) + \rho^{upper}\,\coth(kh_1)}. \tag{43}$$

Relation (43) can be formally derived from (29) by letting $a_1 \to 0$ ($a \neq 0$). Alternatively, it arises from requiring that condition (22) is satisfied by the velocity potentials (17) and (21), thereby ensuring the continuity of normal velocities at the interface.

Remark 7 When the depth of both fluid layers becomes very large ($h, h_1 \to \infty$) the influence of the upper and lower boundaries diminishes, and the dispersion relation (43) for the interface becomes:

$$c^2 = \frac{g}{k}\frac{\rho^{lower} - \rho^{upper}}{\rho^{lower} + \rho^{upper}}.$$

This matches the wavespeed c_2 obtained in (38) in the 'short wave' regime $kh, kh_1 \gg 1$, a physical regime consistent with the 'deep-water' limit. ∎

Remark 8 Relations (39)–(42) pertain to the 'long wave' physical regime, where k is sufficiently small that kh_1, $kh \ll 1$. This regime is consistent with the 'shallow layer' approximation, whereby $h/\lambda, h_1/\lambda \ll 1$ with the depths h, h_1 now assumed to be small. Accordingly, the approximate dispersion relations (39)–(42) are also applicable to the shallow layer regime.

4 Dynamical systems formulation

From the definitions (5), and the solutions (17), (19) we can directly compute expressions for velocity fields in the lower, and upper, fluid layers. If $(x(t), y(t))$ is the path of a particle in the lower-fluid layer Ω^l, then the motion of the particle is described by the nonlinear dynamical system

$$\begin{cases} \dfrac{dx}{dt} = u = a\omega \cos(kx - \omega t) \dfrac{\cosh k(y+h)}{\sinh kh} \\ \dfrac{dy}{dt} = v = a\omega \sin(kx - \omega t) \dfrac{\sinh k(y+h)}{\sinh kh}, \end{cases} \tag{44a}$$

for $-h < y < 0$, with initial data (x_0, y_0). In the upper-fluid layer Ω^u, particle trajectories $(x(t), y(t))$ are determined by the nonlinear dynamical system

$$\begin{cases} \dfrac{dx}{dt} = u_1 = a_1\omega \cos(kx - \omega t) \left\{ \sinh k(y - h_1) + A \cosh k(y - h_1) \right\} \\ \dfrac{dy}{dt} = v_1 = a_1\omega \sin(kx - \omega t) \left\{ \cosh k(y - h_1) + A \sinh k(y - h_1) \right\}, \end{cases} \tag{44b}$$

for $0 < y < h_1$, with initial data (x_0, y_0). The mean-level of the oscillating internal wave interface $y = \eta$ is located at $y = 0$, whereas the free-surface $y = h_1 + \eta_1$ oscillates about the mean-level located at $y = h_1$.

Remark 9 For a given coupled wave motion, the wavenumber k, the frequency ω, and the nondimensional parameter A are fixed constants in the dynamical systems (44a) and (44b). As outlined in some detail in Section 3.3, these are not free-parameters but, rather, they must be determined through solving dispersion relations. Nevertheless, for the illustrative purposes of phase portrait analysis it is beneficial to consider k, ω as fixed constants, while 'allowing' the parameter A to vary in system (44b).

The right-hand sides of the differential systems (44a) and (44b) are smooth, therefore the existence of unique local smooth solutions for both (44a) and (44b) is ensured by the Picard–Lindelöf theorem [38]. Furthermore, since y is bounded, the right-hand sides of (44a) and (44b) are bounded, hence these unique solutions are defined globally [38]. The right-hand sides of both (44a) and (44b) are nonlinear, and thus such systems cannot be solved explicitly. Rather than resorting to further approximations — for instance, through linearising the dynamical systems (44a), (44b) (in the typical mathematical sense [38], rather than the physical sense of Section 2.1) — we will use phase plane analysis to directly establish qualitative features of the solutions. Since the fluid layers are separated by an impermeable interface $y = \eta(x, t)$, and the

solutions (17) and (19) satisfy the matching conditions (14b) at this interface by design, we can address the phase plane analysis of system (44a) in the lower-fluid layer Ω^l, and system (44b) in the upper-fluid layer Ω^u, separately in the first instance, and then piece together the information to get a picture of the motion of the entire two-layer body.

4.1 Phase portrait analysis: lower-fluid layer

The velocity field for the lower-fluid layer (44a) is relatively simple in comparison to that of the upper layer (44b). This difference in complexity is unsurprising given that the lower layer possesses just one moving boundary (the internal wave), whereas the upper layer possesses two (the surface and internal waves). From a mathematical viewpoint, system (44a) is qualitatively identical to that which describes fluid motion in a single homogenous (uniform density) fluid layer whose upper interface separates the fluid from a source of constant pressure (such as the atmosphere). The physical influence of the upper-fluid layer is conveyed implicitly to (44a) by way of the dispersion relations (28) and (29). The motion underlying this type of system was first examined by phase-plane analysis in [12] and, since it offers an accessible illustration of the phase-portrait approach that we implement in more convoluted circumstances in Section 4.2, we include it here.

As we are studying travelling waves, we can transform to a moving frame where the motion is steady by way of the change of variables

$$X(t) = kx(t) - \omega t, \qquad Y(t) = k(y(t) + h), \tag{45}$$

where we recall that $c = \omega/k$. This transforms system (44a) to the following autonomous system

$$\begin{cases} \dfrac{dX}{dt} = M\cos(X)\cosh(Y) - \omega, & \text{(46a)} \\ \dfrac{dY}{dt} = M\sin(X)\sinh(Y), & \text{(46b)} \end{cases}$$

with $(X(0), Y(0)) = (x_0, y_0)$, and where we denote

$$M := \frac{ak\omega}{\sinh(kh)} = \frac{a}{h} \cdot \frac{kh}{\sinh(kh)} \cdot \omega \ll \omega, \tag{47}$$

since $s < \sinh(s)$ for $s > 0$ and $a/h \sim \mathcal{O}(\epsilon) \ll 1$ in the linear wave regime (cf. Section 2.1). Since (46) is periodic in X we focus on the strip $\{X : -\pi \leq X \leq \pi\}$, and the change of variables (45) transforms the lower-fluid

layer to the region $\{Y : 0 \leq Y \leq kh + \mathfrak{e}\cos(X)\}$, where we denote by $\mathfrak{e} = ak$ the *wave-steepness* parameter for the internal interface. The autonomous system (46) meets standard regularity assumptions for the uniqueness of the Cauchy problem [38], therefore its trajectories do not intersect. We note that the right-hand side of (46a) is an even function in both X and Y, while the right-hand side of (46b) is an odd function of both X and Y: therefore the trajectories of (46) have mirror symmetries with respect to both the $X-$ and $Y-$axes.

Remark 10 Without loss of generality, we choose $a > 0$ (hence $M > 0$) throughout this subsection. From direct examination of the dynamical system (46), we see that a change in the sign of M can be effectuated by simply shifting the X variable by π: by From (15a), the difference between choice of signs corresponds physically to choosing either the crest, or the trough, of the internal wave to be located at $X = 0$, respectively.

The 0-isocline is defined to be the set where $dY/dt = 0$, and the ∞-isocline is the set where $dX/dt = 0$. Therefore the 0-isocline is given by the lines $X = 0, \pm\pi$, and the line segment $Y = 0$. The ∞-isocline is given in the region $X \in \left(-\frac{\pi}{2}, \frac{\pi}{2}\right)$ by the curve $(X, \alpha(X))$, where $\alpha(X) \in [Y^*, \infty)$ for $\cosh(Y^*) = \omega/M$, and α is defined as follows: on $\left[0, \frac{\pi}{2}\right)$ we set α to be the inverse of the function $Y \mapsto \arccos\left(\frac{\omega}{M\cosh(Y)}\right)$ defined on $[Y^*, \infty)$, and extend it by mirror symmetry to the interval $\left(-\frac{\pi}{2}, \frac{\pi}{2}\right)$. Since $\frac{\omega}{M\cosh(Y)} \leq 1$ for $Y \geq Y^*$, it follows that α is well-defined; furthermore the even function α is smooth, it takes on its infimum Y^* at $X = 0$, and satisfies the limiting condition $\lim_{X\to\pm\infty} \alpha(X) = \infty$. The only singular point of the system (46) for positive Y is $Q = (0, Y^*)$. To show this is a saddle point we express (46) as a Hamiltonian system

$$\begin{cases} \dot{X} = H_Y, \\ \dot{Y} = -H_X, \end{cases}$$

with the Hamiltonian function $H(X, Y) \equiv M\sinh(Y)\cos(X) - \omega Y$. If (X, Y) is a solution of (46) then $\frac{d}{dt}H(X, Y) = H_X\dot{X} + H_Y\dot{Y} = 0$, and so H is constant along the phase curves. Now Q is a critical point of H, and as the Hessian of H at Q is

$$\begin{pmatrix} -M\sinh(Y^*) & 0 \\ 0 & M\sinh(Y^*) \end{pmatrix},$$

it follows that Q is a nondegenerate singular point. By Morse's lemma [39] in a neighbourhood of Q there exists a diffeomorphic change of coordinates which sends the level lines of H to hyperbolas. Thus Q is a saddle point for H. Away from the critical point Q the seperatrix $H^{-1}\{H(Q)\} = \{(X, Y) :$

$H(X,Y) = H(Q)\}$ is a smooth curve, by the implicit function theorem, and it intersects the vertical line $X = \pi$ at the point (π, β) where β is implicitly defined by the equation $H(\pi,\beta) = -M\sinh(\beta) - \omega\beta = H(Q)$. For $X \in (\frac{\pi}{2}, \pi)$ we have $dX/dt < 0$, $dY/dt > 0$. If $X \in (0, \frac{\pi}{2})$ then $dX/dt < 0$ below the curve of $\alpha(X)$ and is positive above it, while dY/dt remains positive in this region. The corresponding signs for $X \in (-\pi, 0)$ are obtained using symmetry with respect to the Y-axis. A phase portrait for the lower-fluid layer is given in Figure 3.

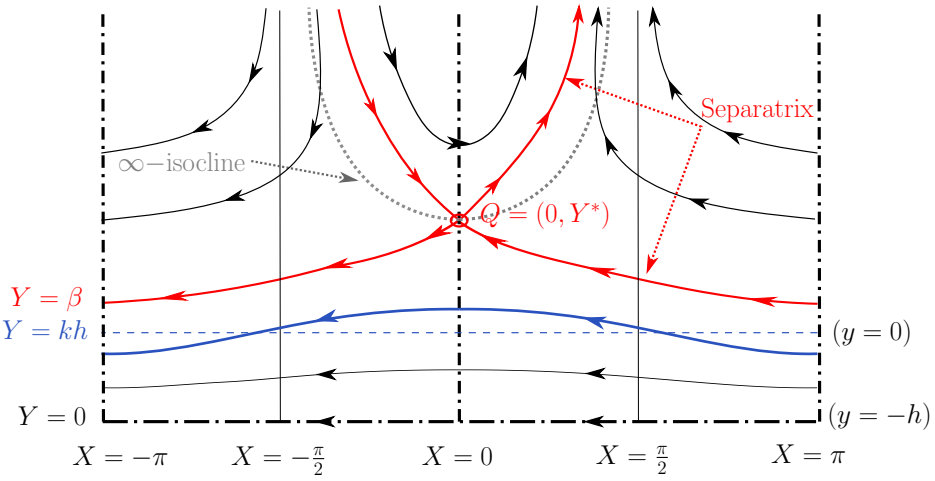


Figure 3: Phase portrait for the lower-fluid layer. The dotted grey line ····· represents the $\infty-$isocline, with the dotted-dashed lines -·-·- representing the $0-$isoclines. The internal wave profile (——) with mean-water level $Y = kh$ (corresponding to $y = 0$) is also illustrated.

To conclude our discussion of the phase plane diagram for the lower-fluid layer we consider an additional restriction necessary to ensure that the system (50), and the resulting phase portrait, are compatible with the physical model. Namely, the streamline which represents the internal-wave must lie beneath the separatrix. This is ensured if the wave-trough is located beneath $Y = \beta$ at $X = \pi$, that is, if $k(h-a) < \beta$. However, since β is not prescribed explicitly, it is more expedient to instead examine the wave-crest which, by (15a) and (45), is located at $(X,Y) = (0, k(h+a))$. Therefore we require $k(h+a) < Y^*$ or, equivalently,

$$\tilde{\epsilon} \cdot \cosh\left(kh\left(1+\tilde{\epsilon}\right)\right) \leq \frac{\sinh(kh)}{kh}. \tag{48}$$

Here we denote the non-dimensional parameter $\tilde{\epsilon} := a/h$. Condition (48) features an interplay between physical parameters such as the wavenumber

$k = 2\pi/\lambda$, the mean-depth h of the lower-fluid layer Ω^l, and the internal wave amplitude a. In the limiting regime $kh \to 0$, which corresponds to a shallow fluid-layer (or long wave) approximation, we have $\sinh(kh)/kh \to 1$. Hence (48) holds if $\tilde{\epsilon}\cosh(kh(1+\tilde{\epsilon})) \approx \tilde{\epsilon} < 1$: this condition is intrinsically satisfied in the linear wave regime where $\tilde{\epsilon} \sim \mathcal{O}(\epsilon) \ll 1$ (cf. Section 2.1). For $kh \to \infty$, which corresponds to a deep fluid-layer (or short wave) approximation, we have $\tanh(kh) \to 1$, hence relation (48) holds if $\mathfrak{e} < 1$. This condition holds irrevocably for linear water waves since $\mathfrak{e} = \epsilon \cdot \delta \ll 1$ (cf. Section 2.1). In general, if condition (48) holds then $\tilde{\epsilon} < \tanh(kh)/kh$ which, for given values of h and k, offers a quantifiable measure of how small the amplitude a must be in order for linear wave solutions to exist, and be physically valid.

4.2 Phase portrait analysis: upper-fluid layer

As in the previous section, we work in a moving frame by making the change of variables

$$X(t) = kx(t) - \omega t, \qquad Y_1(t) = k(h_1 - y(t)), \tag{49}$$

which transforms system (44b) to the autonomous system

$$\begin{cases} \dfrac{dX}{dt} = F(X, Y_1) := M_1 A\cos(X)\cosh(Y_1) - M_1\cos(X)\sinh(Y_1) - \omega \\ \dfrac{dY_1}{dt} = G(X, Y_1) := M_1 A\sin(X)\sinh(Y_1) - M_1\sin(X)\cosh(Y_1), \end{cases} \tag{50}$$

where we denote the parameter $M_1 = a_1 k\omega$ and A is given by (20). As (50) is periodic in X we need only consider the strip $\{X : -\pi \leq X \leq \pi\}$ and, due to the definition of the Y_1 in (49), the physically–relevant solutions of (50) will be located in the region $\{Y_1 : -\mathfrak{e}_1\cos(X) \leq Y_1 \leq kh_1 - \mathfrak{e}\cos(X)\}$, where we denote by $\mathfrak{e}_1 = a_1 k = 2\pi \cdot a_1/\lambda$ the *wave-steepness* parameter for the surface. This non-dimensional parameter can be expressed $\mathfrak{e}_1 = 2\pi \cdot \delta \cdot \epsilon_1$ in terms of the wave-amplitude parameter ϵ_1, and shallowness parameter δ: accordingly $\mathfrak{e}_1 \ll 1$ (cf. Section 2.1). We note that $M_1 \ll \omega$ since $M_1/\omega = \mathfrak{e}_1$. The autonomous system (50) meets the standard regularity assumptions for the uniqueness of the Cauchy problem [38], therefore its trajectories do not intersect. Moreover, since $F(X, Y_1)$ is an even function, and $G(X, Y_1)$ an odd function, with respect to X, any trajectory of system (50) is symmetric with respect to the Y_1-axis when viewed as a curve in the $(X, Y_1)-$phase plane. It is expedient to further re-express the right-hand sides of (50) as

$$F(X, Y_1) = M_1\cos(X)f(Y_1) - \omega, \quad G(X, Y_1) = M_1\sin(X)g(Y_1), \tag{51a}$$

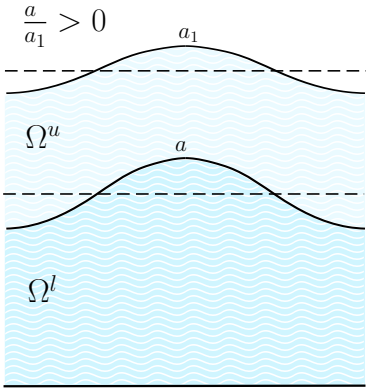
where we define the functions

$$f(Y_1) := A\cosh(Y_1) - \sinh(Y_1), \quad g(Y_1) := A\sinh(Y_1) - \cosh(Y_1). \tag{51b}$$

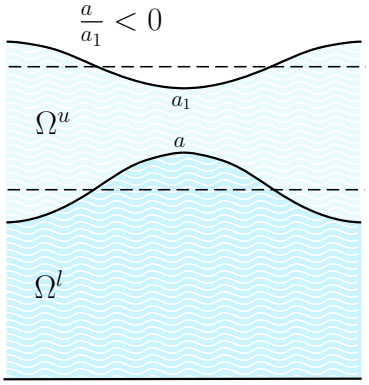
Note that $f'(Y_1) = g(Y_1)$, and $g'(Y_1) = f(Y_1)$, where $(\cdot)'$ denotes differentiation with respect to Y_1. In order to investigate the phase portrait of system (50) we must begin by investigating the 0-isocline (defined as the set of points where the vector field is horizontal, $\dot{Y}_1 = 0$, and so $G(X, Y_1) = 0$ in (51a)) and the ∞-isocline (defined as the set of points where the vector field is vertical, $\dot{X} = 0$, and so $F(X, Y_1) = 0$ in (51a)).

Remark 11 The change of variables (49) reflects vertical coordinates through the line $y = h_1$ with the effect that, when represented in terms of the Y_1 variable, wave crests correspond to troughs, and troughs to crests. Additionally, when expressed in terms of the Y_1 variable, the streamline denoting the surface wave lies *beneath* that of the internal wave.

Remark 12 The sign of the parameter M_1 matches the sign of a_1, the amplitude of the surface water wave. From (15b), whether a_1 is positive, or negative, determines physically whether the crest, or the trough, of the surface wave is located at $X = 0$, respectively. The sign of the ratio a/a_1 ascertains whether the surface and internal waves are coupled in-phase, or out-of-phase, a key characteristic in determining the qualitative nature of system (50). The value of the parameter A prescribes, by way of (23), the sign of this ratio. Without loss of generality, we fix $M_1 > 0$ (and hence $a_1 > 0$) throughout subsequent considerations, with the sign of a consequently matching that of the ratio a/a_1 as prescribed by A.



(a) In-phase waves can occur for $A < 1$, $A = 1$, and $A > 1$.



(b) Out-of-phase waves occur only for values $A > 1$.

In Remark 1 we noted that for every linear coupled wave system of the form (15) one of the roots of (31), A_2, is always greater than one: this solution constitutes an out-of-phase wave system. The other root, A_1, represents an in-phase wave system and, depending on the physical parameters of the problem being considered, A_1 may be greater than, less than, or equal to one. It turns out that the dynamical system (50) potentially generates three qualitatively different fluid motions, depending on whether $A < 1$, $A = 1$, and $A > 1$. This is due to the qualitatively different behaviour of the $f(Y_1), g(Y_1)$ functions defined in (51b) for these values of A. Accordingly, we treat each case separately.

4.2.1 System (50) with $A < 1$:

Direct computation in (51b) shows that $g(Y_1)$ is negative, takes its maximum at

$$\bar{Y_1} = \frac{1}{2} \ln \left(\frac{A+1}{1-A} \right), \tag{52}$$

and $\lim_{Y_1 \to +\infty} g(Y_1) = -\infty$. Hence $G(X, Y_1) < 0$ for $0 < X < \pi$ and vanishes at $X = 0$ and $X = \pi$: the $0-$isocline for system (50) in $[0, \pi]$ is composed of the two vertical lines $X = \{0, \pi\}$.

To determine the $\infty-$isocline we examine $f(Y_1)$ for $A < 1$. In this setting it follows directly from (51b), and the fact $f'(Y_1) = g(Y_1)$, that f is monotone decreasing, with $f(0) = A$, $f(\bar{Y_1}) = 0$, and where $\lim_{Y_1 \to -\infty} f(Y_1) = \infty$, $\lim_{Y_1 \to +\infty} f(Y_1) = -\infty$; a schematic for $f(Y_1)$ is given as follows.

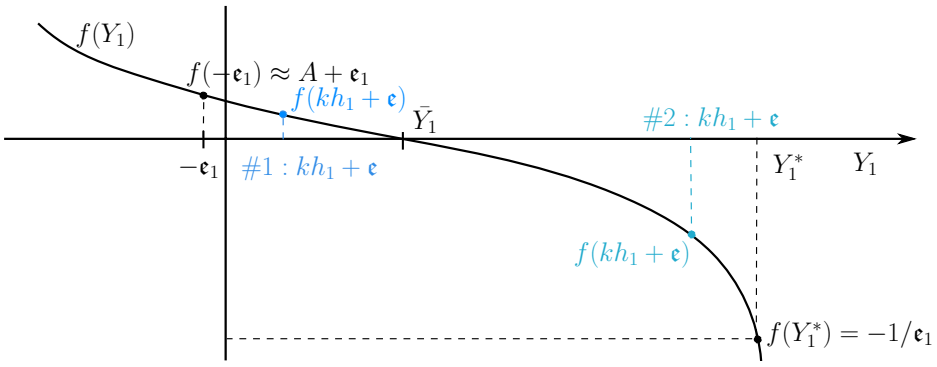


Figure 4: Schematic of $f(Y_1)$ for $A < 1$. $f(0) = A = \tanh(\bar{Y_1})$

Remark 13 We note that the value $\bar{Y_1}$ where $f(\bar{Y_1}) = 0$, as determined by (52), is well-defined for $A < 1$, and corresponds to $A = \tanh(\bar{Y_1})$: it follows that $A \to 0 \Leftrightarrow \bar{Y_1} \to 0$, while $A \to 1 \Leftrightarrow \bar{Y_1} \to \infty$. Figure 4 displays two

possible scenario for the location of the internal interface, namely: Case 1, where $kh_1+\mathfrak{e} \leq \bar{Y_1}$; Case 2, where $kh_1+\mathfrak{e} > \bar{Y_1}$. For illustrative purposes, we note that $\bar{Y_1} = 0.31$ for $A = 0.3$; $\bar{Y_1} = 0.69$ for $A = 0.6$; $\bar{Y_1} = 1.47$ for $A = 0.9$; $\bar{Y_1} = 2.65$ for $A = 0.99$; $\bar{Y_1} = 3.8$ for $A = 0.999$. While the phase portraits for system (50) are qualitatively similar in either case, we will see in Section 5 that particle trajectories are distinctly different for the two different choices.

The $\infty-$isocline occurs in the region $0 \leq X \leq \frac{\pi}{2}$ if $f(\tilde{Y_1}^*) = 1/\mathfrak{e}_1 > 0$ for some value of $\tilde{Y_1}^*$. The maximum positive value that f attains in the upper-fluid layer (where $-\mathfrak{e}_1 \leq Y_1 \leq kh_1 + \mathfrak{e}$) is $f(-\mathfrak{e}_1) \approx A + \mathfrak{e}_1 \lessapprox 1$ (cf. Figure 4) which means, since $1/\mathfrak{e}_1 \gg 1$, that the $\infty-$isocline (and associated singular point $\tilde{Q}$) in this region will not have any influence on our physical solution: nevertheless we include it in our picture for completeness. In the region $\frac{\pi}{2} < X \leq \pi$, we observe that at $X = \pi$ there exists ${Y_1}^* > \bar{Y_1}$ such that $f({Y_1}^*) = -\omega/M_1 = -1/\mathfrak{e}_1$: $Q_1(\pi, {Y_1}^*)$ is a singular point and the ∞-isocline, which lies in the interval $\left(\frac{\pi}{2}, \pi\right]$, takes its minimum at $Q(\pi, {Y_1}^*)$ and tends to $+\infty$ when $X \to \frac{\pi}{2}^+$. By symmetry, there is an $\infty-$isocline in the interval $\left[-\pi, -\frac{\pi}{2}\right)$ which takes its minimum at $\mathfrak{Q}_1 = (-\pi, Y_1^*)$, and which tends to ∞ as $X \to \frac{3\pi}{2}^-$. To ascertain the nature of the singular point Q_1 (and, by periodicity, $\mathfrak{Q}_1$) we observe that system (50) has a Hamiltonian structure, for the Hamiltonian

$$H_1(X, Y_1) = M_1 A \cos(X) \sinh(Y_1) - \omega Y_1 - M_1 \cos(X) \cosh(Y_1). \tag{53}$$

Since Q_1 is a critical point of H_1, and the Hessian at Q_1 is given by

$$\begin{pmatrix} M_1 A \sinh(Y_1^*) - M_1 \cosh(Y_1^*) & 0 \\ 0 & -(M_1 A \sinh(Y_1^*) - M_1 \cosh(Y_1^*)) \end{pmatrix},$$

it follows by Morse's lemma [39] that Q_1 is a saddle point which lies at the intersection of four separatrices: two that reach Q_1 in infinite time in the future, and two that need infinite time backwards to reach the saddle point. Given the $0-$ and $\infty-$isoclines, the signs of the vector field components $F(X, Y_1)$ and $G(X, Y_1)$ for system (50) are easily determined, leading to the phase portrait in Figure 5.

For the parameter value $A < 1$, considerations of Section 3.3 (specifically relations (34) and (36)) dictate that the surface and interface waves should be in-phase: this is indeed borne out by the phase-portrait in Figure 5. In order that system (50) describes physically–relevant solutions, the singular point Q_1 (and its periodic image $\mathfrak{Q}_1$) must lie beneath the internal wave profile in terms of physical coordinates, or above the interface in terms of Y_1 coordinates. Hence we require $kh_1 + \mathfrak{e} < Y_1^*$ or, equivalently (cf. Figure 4)

$$f(kh_1 + \mathfrak{e}) > -1/\mathfrak{e}_1. \tag{54}$$

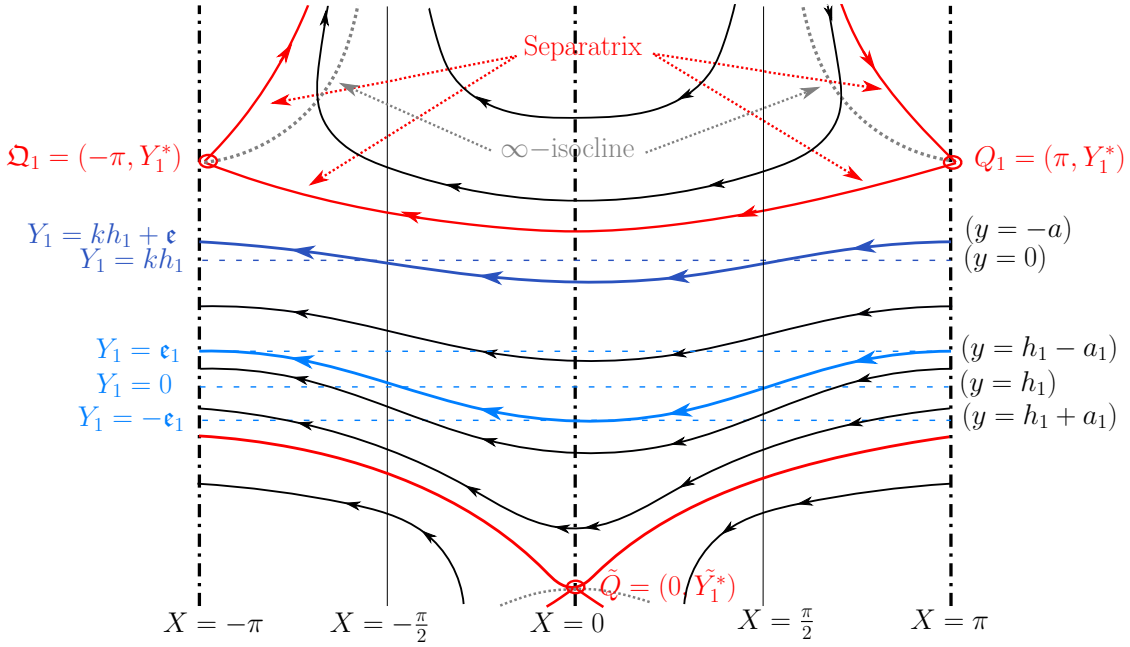


Figure 5: Phase portrait of the upper-fluid layer when $A < 1$. The dotted grey lines ····· represent the $\infty-$isoclines, while the dotted-dashed lines -·-·- represent the $0-$isoclines. The surface wave profile (——) has mean-water level $Y_1 = 0$, corresponding to $y = h_1$. The internal wave profile (——) has mean water level $Y = kh_1$, corresponding to $y = 0$.

4.2.2 System (50) with $A = 1$:

For $A = 1$, the relations in (51b) reduce to $f(Y_1) = e^{-Y_1} = -g(Y_1)$. Accordingly, the phase portrait for positive values of Y_1 rapidly converges to a series of flat, horizontal lines as Y_1 increases, since the velocity field converges exponentially fast to the uniform system $\dot{X} \equiv -\omega$ and $\dot{Y}_1 \equiv 0$. We have $G(X, Y_1) < 0$ for $0 < X < \pi$ and vanishes at $X = 0$ and $X = \pi$, hence these vertical lines comprise the $0-$isocline for system (50) in $[0, \pi]$. The $\infty-$isocline consists of points Y_1 where $\cos(X)e^{-Y_1} = 1/\mathfrak{e}_1$, and for $X \in \left[\frac{\pi}{2}, \pi\right]$ there is no such solution. For each $X \in \left[0, \frac{\pi}{2}\right)$ there is a solution, and for $X = 0$ we have $e^{-Y_1^*} = 1/\mathfrak{e}_1$ for $Y_1^* = -\ln(1/\mathfrak{e}_1)$. The point $Q_1 = (0, Y_1^*)$ is a singular point, and since the Hessian of the Hamiltonian (53) is

$$M_1 \begin{pmatrix} e^{Y_1^*} & 0 \\ 0 & -e^{Y_1^*} \end{pmatrix},$$

it follows immediately that Q_1 is a saddle point which lies at the confluence of four separatrices. The maximum value of the $\infty-$isocline is located at Q_1, and it decreases monotonically to $-\infty$ as $X \to \frac{\pi}{2}$. The phase portrait for system (50) when $A = 1$ is given in Figure 6.

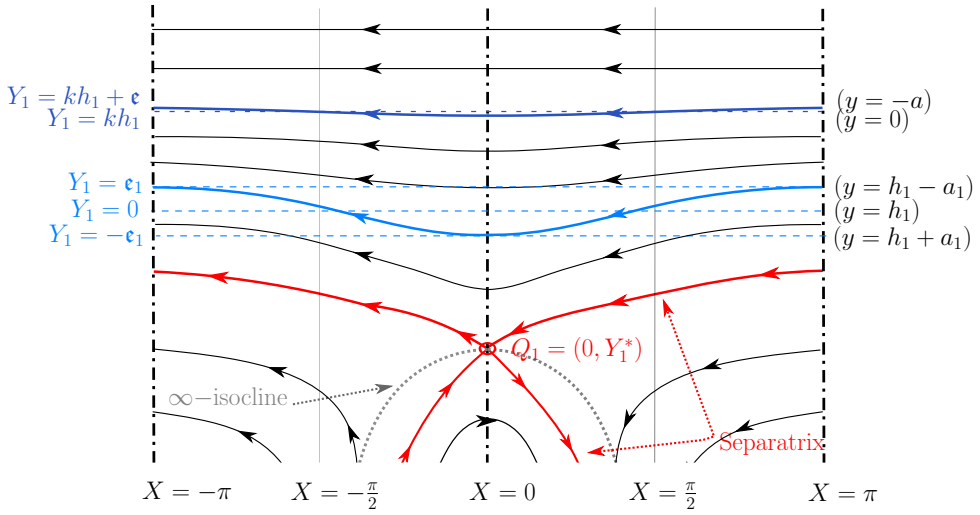


Figure 6: Phase portrait of the upper-fluid layer when $A = 1$. The dotted grey line ····· represents the $\infty-$isocline, while the dotted-dashed lines -·-·- represent the $0-$isoclines. The surface wave profile (——) has mean-water level $Y_1 = 0$, corresponding to $y = h_1$. The internal wave profile (——) has mean water level $Y = kh_1$, corresponding to $y = 0$.

For the parameter value $A = 1$, relations (34) and (36) imply that the surface and interface waves should be in-phase. This is consistent with the phase-portrait in Figure 6. We note that the the surface-wave streamline must be located above the separatrix for physically–relevant solutions of (50), and this is the case for $-\mathfrak{e}_1 > Y_1^*$, that is,

$$\mathfrak{e}_1 e^{\mathfrak{e}_1} < 1. \tag{55}$$

4.2.3 System (50) with $A > 1$:

To ascertain the $0-$isocline we must determine when $G(X, Y_1) = 0$ in (51a). Firstly, it is obvious from (51a) that this occurs when $X = 0$ and $X = \pi$. From direct computation in (51b) we have $g(0) = -1$, while $g'(Y_1) > 0$ and $\lim_{Y_1 \to +\infty} g(Y_1) = +\infty$ whenever $A > 1$. Hence, there exists a unique $\bar{Y}_1$ such

that $g(\bar{Y}_1) = 0$, and we can calculate it directly to get

$$\bar{Y}_1 = \frac{1}{2} \ln \left(\frac{A+1}{A-1} \right). \tag{56}$$

Hence, the $0-$isocline is composed of the vertical half-lines $X = 0$, $X = \pi$, and the horizontal line-segment $Y_1 = \bar{Y}_1$. The value for $\bar{Y}_1$ as determined by (56), which is well-defined for $A > 1$, corresponds to $A = \coth(\bar{Y}_1)$; it follows that $A \to 1 \Leftrightarrow \bar{Y}_1 \to \infty$, while $A \to \infty \Leftrightarrow \bar{Y}_1 \to 0$. As we elucidate below, and in Section 5 when characterising qualitative features of the underlying fluid dynamics, the precise value of $\bar{Y}_1$ plays a pivotal role in physical considerations.

The study of the ∞-isocline, where $F(X, Y_1) = 0$ in (51a), can be achieved through examining $f(Y_1)$ in (51b). We have $f(Y_1) > 0$, $f(0) = A$, and $\lim_{Y_1 \to +\infty} f(Y_1) = +\infty$ since $A > 1$. It follows from $f'(Y_1) = g(Y_1)$ that the function f has a minimum at $Y_1 = \bar{Y}_1$, which can be calculated to get $f(\bar{Y}_1) = 1/\sinh(\bar{Y}_1) < A$. We note that when $A \to \infty$ the minimum value $f(\bar{Y}_1)$ tends to A, with both values becoming infinite; when $A \to 1$ the minimum of f tends to zero, which follows from (51b) since $\lim_{A \to 1} f(Y_1) = e^{-Y_1}$. Furthermore, if $\hat{Y}_1 > \bar{Y}_1$ is the unique value such that $f(\hat{Y}_1) = A$, then the function $f(Y_1)$ is invertible on the set $Y_1 \in (\hat{Y}_1, \infty)$; a schematic for $f(Y_1)$ is given in Figure 7.

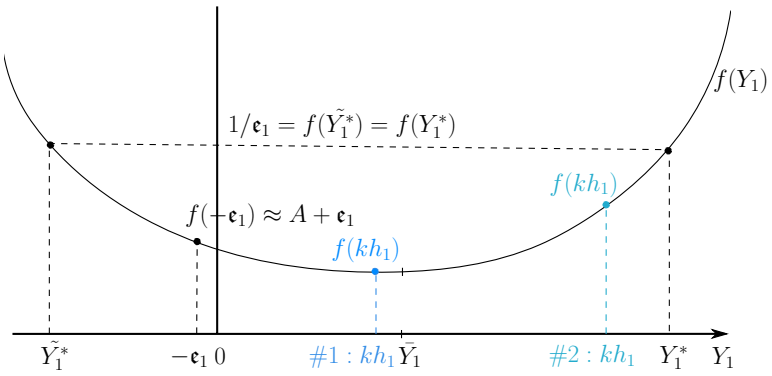


Figure 7: Schematic of $f(Y_1)$ for $A > 1$, where $f(0) = A$, with $A = \cosh(\bar{Y}_1)/\sinh(\bar{Y}_1)$, and the minimum value attained is $f(\bar{Y}_1) = 1/\sinh(\bar{Y}_1)$.

For $\leq \frac{\pi}{2} \leq X \leq \pi$, $F(X, Y_1)$ is strictly positive since $M_1 > 0$, hence there are no ∞-isocline or singular points in this region. In the region $0 \leq X < \frac{\pi}{2}$, the ∞-isocline is given by points (X, Y_1) where $\cos(X) f(Y_1) = \omega/M_1 = 1/\mathfrak{e}_1$, therefore, since the left-hand side is maximised at $X = 0$, an $\infty-$isocline exists in this region if $f(Y_1^*) = 1/\mathfrak{e}_1$ for some value of Y_1^*.

It follows from the schematic in Figure 7 that, if $\mathfrak{e}_1 < \max_{Y_1} 1/f(Y_1) = \sinh(\bar{Y_1})$, there exists a pair of values, $\tilde{Y_1^*}$, Y_1^* with $\tilde{Y_1^*} \leq Y_1^*$, say, such that $f(Y_1^*) = f(\tilde{Y_1^*}) = 1/\mathfrak{e}_1$. We denote these singular points of the system (50) by $\tilde{Q_1} = (\pi, \tilde{Y_1^*})$, $Q_1 = (\pi, Y_1^*)$, and let us first examine the point Q_1. By virtue of the properties of $f(Y_1)$, the ∞-isocline is given in the interval $X \in \left[0, \frac{\pi}{2}\right)$ by the curve $(X, \alpha_1(X))$, where $\alpha_1(X) : \left[0, \frac{\pi}{2}\right) \to [{Y_1}^*, +\infty)$ is the inverse of the function $f(Y_1)$ restricted to the interval $[{Y_1}^*, +\infty)$. We note that $\alpha_1(0) = {Y_1}^*, \lim_{X \to \frac{\pi}{2}+} \alpha_1(X) = +\infty$ and, in the interval $\left[0, \frac{\pi}{2}\right)$, α_1 is an increasing function. Given the Hamiltonian (53) for system (50), the Hessian at Q_1 is

$$\begin{pmatrix} M_1 \cosh(Y_1^*) - M_1 A \sinh(Y_1^*) & 0 \\ 0 & -(M_1 \cosh(Y_1^*) - M_1 A \sinh(Y_1^*)) \end{pmatrix},$$

and arguments similar to those above involving Morse theory imply that Q_1 is a saddle point which lies at the intersection of four separatrices: two that reach Q_1 in infinite time in the future, and two that need infinite time backwards to reach the saddle point. Analogous reasoning hows that the singular point $\tilde{Q_1}$ is also a saddle point, and the $\infty-$isocline emanating from $\tilde{Q_1}$ is qualitatively similar to that described for Q_1, except 'flipped' vertically. Having characterised the $0-$ and $\infty-$isoclines, we can easily determine the signs of the two components $F(X, Y_1)$ and $G(X, Y_1)$ of the vector field given by system (50), and employing symmetry properties of (50) we infer the phase portrait behaviour in the region $-\pi \leq X \leq 0$. The complete phase portrait of system (50) is given in Figure 8.

The surface wave profile has a mean-water level $Y_1 = 0$, which corresponds to $y = h_1$, while the internal wave profile has a mean water level $Y = kh_1$, which corresponds to $y = 0$. From the phase portrait in Figure 8 we see that there are two qualitatively different fluid motions possible in the upper-fluid layer, which depends on the location of $Y = kh_1$.

In Case 1, $kh_1 \leq \bar{Y_1}$ and the internal wave profile is in-phase with the surface wave: in this case, all streamlines have their crests located at $X = 0$. If $kh_1 = \bar{Y_1}$ then we see from Figure 8 that the motion is restricted to a horizontal line and the internal interface is flat: $\mathfrak{e} = 0$ in this scenario (this also follows from (23) and (56), which imply that $a = 0$ for $kh_1 = \bar{Y_1}$). We note that whenever $kh_1 \leq \bar{Y_1}$ there is an additional bound on $\mathfrak{e}$, namely $\mathfrak{e} < kh_1 - \bar{Y_1}$. In Case 2, $kh_1 > \bar{Y_1}$ and the internal wave is now out-of-phase with the surface wave. In this scenario, all streamlines beneath the line $Y_1 = \bar{Y_1}$ have their crest located at $X = 0$, with the amplitudes diminishing steadily until they vanish at the $0-$isocline $Y_1 = \bar{Y_1}$. As we move above $Y_1 = \bar{Y_1}$ the amplitude of the streamlines increase steadily, until the reach

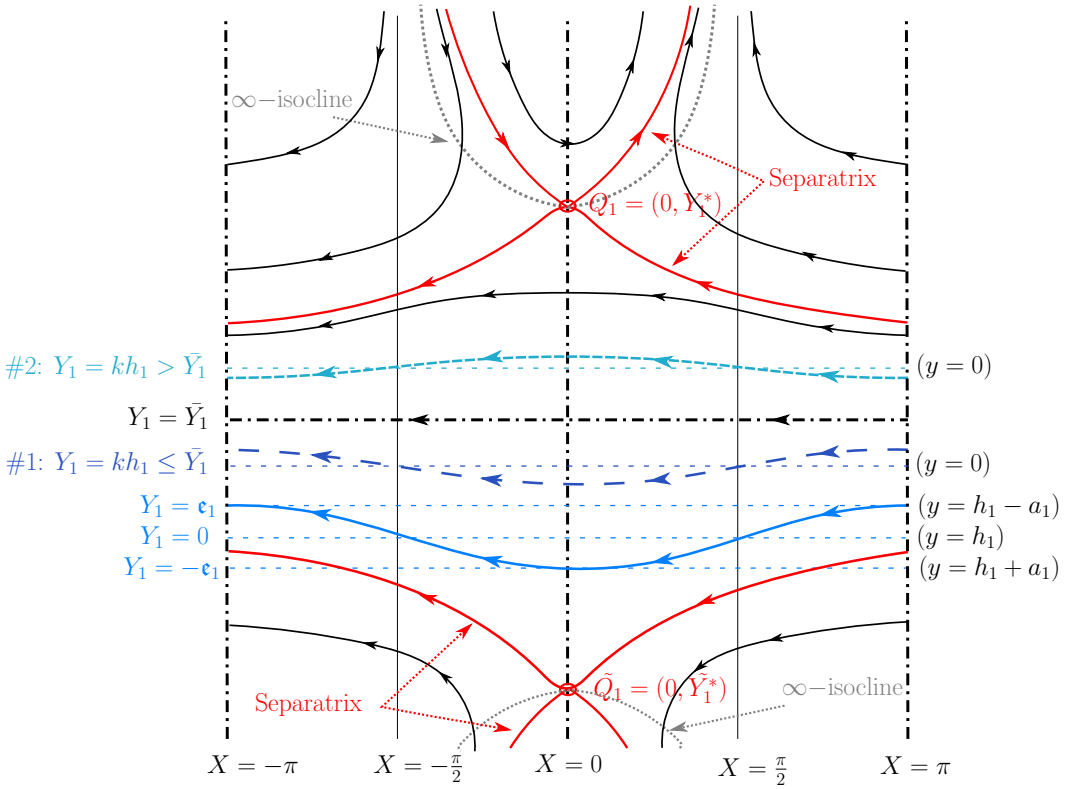


Figure 8: Phase portrait for the upper-fluid layer when $A > 1$. The dotted grey lines ····· represent the $\infty-$isoclines, with the dotted-dashed lines -·-·- representing the $0-$isoclines. The surface wave profile (——) has mean-water level $Y_1 = 0$, corresponding to $y = h_1$. The internal wave profile is illustrated for two differing values of the mean water level $Y = kh_1$, corresponding to $y = 0$: $kh_1 \leq \bar{Y}_1$ in Case 1 (– –), whereas $kh_1 > \bar{Y}_1$ for Case 2 (----).

a maximum at $Y_1 = kh_1$, which corresponds to the internal wave profile. However, the vertical velocity reverses direction as we pass $Y_1 = \bar{Y}_1$, and so the line $X = 0$ now corresponds to the wave trough.

This phase-plane analysis is congruent with the deductions made in Section 3.3 through the consideration of dispersion relations. For the parameter value $A > 1$, relations (34) and (36)) permit the existence of both in-phase, and out-of-phase, surface and interface waves: this is indeed borne out by the phase-portrait in Figure 5. In particular, for Case 1, by (56) we have $A = \coth(\bar{Y}_1) \leq \coth(kh_1)$, which implies, by (34), that $A = A_1$ and so waves must be in-phase by (36). Conversely, for Case 2, again by (56) we have $A = \coth(\bar{Y}_1) \geq \coth(kh_1)$, which implies, by (34), that $A = A_2$ and so these

waves must be out-of-phase by (36).

In order for system (50) to describe physically–relevant solutions, the singular points $\tilde{Q}_1$ and Q_1 must lie outside the upper-fluid layer, hence we must have $\tilde{Y_1}^* < -\mathfrak{e}_1$ and $kh_1 + \mathfrak{e} < Y_1^*$ or, equivalently (cf. Figure 7),

$$\max\{f(-\mathfrak{e}_1), f(kh_1 + \mathfrak{e})\} < 1/\mathfrak{e}_1. \tag{57}$$

Since $\mathfrak{e}_1 \ll 1$ in the linear regime, the only way this condition could breakdown is for A to be sufficiently large (and $\bar{Y_1}$ to be correspondingly small), cf. Figure 7 and the discussions. Since $f(-\mathfrak{e}_1) \approx A + \mathfrak{e}_1$, if condition (57) holds we must have

$$\mathfrak{e}_1^2 + A\mathfrak{e}_1 \approx A\mathfrak{e}_1 < 1,$$

Remark 14 Although not lying within the physical regime, we note that in the limit $1/\mathfrak{e}_1 \to \sinh(\bar{Y_1})^+$ the two singular points $\tilde{Q}_1$ and Q_1 coalesce, with $\tilde{Y_1}^* \to \bar{Y_1}^-$, $Y_1^* \to \bar{Y_1}^+$. In the process, the two singular points converge at $(0, \bar{Y_1})$, and when $1/\mathfrak{e}_1 = \sinh(\bar{Y_1})$ the respective horizontal separatrices of these singular points merge to coincide with the line $Y_1 = \bar{Y_1}$, and the $\infty-$isoclines 'intersect'. Hence $(0, \bar{Y_1})$ is a bifurcation point when $1/\mathfrak{e}_1 = \sinh(\bar{Y_1})$, and it is interesting from the mathematical point of view to discuss this phenomenon as $\mathfrak{e}_1$ increases. In this case $1/\mathfrak{e}_1 < \sinh(\bar{Y_1})$ and $(0, \bar{Y_1})$ is a degenerate saddle, with bifurcation occurring along the line $Y_1 = \bar{Y_1}$ as two singular points are created from $(0, \bar{Y_1})$: one moving in the decreasing $X-$direction, as well as a dual one moving in the increasing $X-$direction (by virtue of symmetry with respect to the Y_1-axis). In summary, as $\mathfrak{e}_1$ decreases $(1/\mathfrak{e}_1 > \sinh(\bar{Y_1}))$, bifurcation occurs at $(0, \bar{Y_1})$ with singular points moving along the Y_1-axis; whereas when $\mathfrak{e}_1$ increases $(1/\mathfrak{e}_1 < \sinh(\bar{Y_1}))$ the singular points bifurcate along the line $Y_1 = \bar{Y_1}$. Both lines are actually branches of the $0-$isocline, as is shown in Figure 8.

5 Particle trajectories

In this section we pursue a Lagrangian description of fluid motion, proving results concerning particle trajectories expressed in terms of the physical coordinates. Firstly, we prove that there does not exist any closed particle paths in either the lower, or upper, fluid layers (equivalently, neither the system (44a), nor (44b), prescribe any fluid particle trajectories $(x(t), y(t))$ which are periodic). Indeed, we establish that all particles experience a forward drift. Wave-induced mean-flows have been the focus of systematic investigation since the observation of Stokes (1847) that fluid particles experience a mean net drift velocity in the direction of wave motion for surface waves.

However, the Stokes' drift phenomenon is intrinsically nonlinear (cf. [26, 44]) since fluid drift occurs at order $\mathfrak{e}^2$, where $\mathfrak{e}$ relates to the wave steepness. In this section we establish that all particles undergoing fluid motion induced by *linear* coupled surface and internal waves experience a forward drift. Following this, we provide a complete qualitative description of particle motion in both fluid layers: our analysis reveal some complex, and surprising, particle trajectory patterns in the upper fluid layer. It has commonly been assumed (cf. [1]) that fluid particles undertake an orbital motion for internal waves, which is greatest at the pycnocline, and we demonstrate that this is not always the case. Finally, we establish monotonicity properties for the forward drift experienced by fluid particles for a range of possible physical scenarios.

In Section 4.1 we constructed phase portraits for systems (46) and (50), which describe fluid motion in the lower- and upper-fluid layers, respectively. The analysis is performed in terms of the $(X, Y)-$ and $(X, Y_1)-$variables, which pertain to moving reference frames travelling horizontally with speed c with respect to the original physical coordinates (x, y). From the phase portraits in Figures 3, 5, 6, 8 we have determined the physically-admissible fluid trajectories in each fluid layer. In particular, if we suppose that $(X(t), Y(t))$ is a solution of (46) in the lower-fluid layer with initial value $(X(0), Y(0)) = (\pi, Y^0)$, then focus is restricted to $Y^0 \in [0, k(h-a)]$. Correspondingly, if $(X(t), Y_1(t))$ is a solution to (50) in the upper-fluid layer with $(X(0), Y_1(0)) = (\pi, Y_1^0)$, then $Y_1^0 \in [\mathfrak{e}_1, kh_1 + \mathfrak{e}]$ if $a/a_1 > 0$, whereas $Y_1^0 \in [\mathfrak{e}_1, kh_1 - \mathfrak{e}]$ if $a/a_1 < 0$. Furthermore, as motion is steady in the moving frames it follows that fluid particle trajectories coincide with the streamlines (note that $\dot{X} < 0$ uniformly along fluid streamlines in the moving frames) and a complete qualitative picture of fluid motion may be ascertained. That a comprehensive description of the underlying fluid motion is achievable in this setting is primarily due to (46) and (50) being autonomous systems.

When formulated in terms of the physical coordinates (x, y) in a fixed reference frame, it is more difficult to elucidate the properties of the underlying fluid motion. This is hardly surprising since motion in the lower- and upper-fluid layers is described now by nonautonomous systems, (44a) and (44b), respectively. Nevertheless, we may use properties established during the phase-portrait analysis of Section 4.1 to infer a physical description of fluid motion by reversing the coordinate transformations (45), and (49), using

$$x(t) = \frac{X(t)}{k} + ct, \quad y(t) = \frac{Y(t)}{k} - h, \tag{58}$$

in the lower-fluid layer, and

$$x(t) = \frac{X(t)}{k} + ct, \quad y(t) = h_1 - \frac{Y_1(t)}{k}. \tag{59}$$

in the upper-fluid layer, respectively. Note that the reflection term involved in the vertical coordinate transformation in (59) reverses the vertical orientation of fluid motion when expressed in terms of the physical coordinate y, as opposed to the Y_1 coordinate.

The next lemma is stated for motion in the lower fluid layer, but applies similarly to fluid motion in the upper layer. Suppose $(X(t), Y(t))$ describes a streamline in the lower-fluid layer such that $(X(0), Y(0)) = (\pi, Y^0)$, and let $t_{Y^0}(-\pi)$ denote the time it takes for the particle to intersect the line $X = -\pi$.

Lemma 5.1 *If the particle trajectory prescribed by $(x(t), y(t))$ is a closed path with period τ then, necessarily, we have $\tau = \frac{2\pi}{\omega}$. Conversely, suppose $t_{Y^0}(-\pi) = \frac{2\pi}{\omega}$, then the particle path prescribed by $(x(t), y(t))$ is closed.*

Proof The proof follows from the periodicity of the system (46), or (50), with respect to X, together with the definitions (58) and (59)— cf. [12] for proof of a similar result.

5.1 Lower-fluid layer

The main result for motion in the lower-fluid layer is stated as follows.

Theorem 5.2 *The system* (44a) *has no solutions $(x(t), y(t))$ which are periodic. Accordingly, there are no closed particle paths in the lower-fluid layer, instead all fluid particles experience a positive horizontal drift.*

System (44a) is qualitatively similar to one which describes motion of a surface wave propagating on a single homogeneous fluid layer of finite depth. Accordingly, the proof of Theorem 5.2 runs along the lines of analysis first performed in [12]. For the sake of completeness, and as a useful comparison with the more complex motion of the upper-fluid layer, we present a proof.

Proof Bearing in mind Lemma 5.1, it suffices to show that $t_{Y^0}(-\pi) > \frac{2\pi}{\omega}$ in order to prove the theorem. We start with the case $Y^0 = 0$, where the streamline is located on the flat bed and so $Y(t) \equiv 0$ and $X(t)$ can be explicitly obtained by solving $\dot{X} = M\cos(X) - \omega$, with $X(0) = \pi$. It follows that

$$t_0(-\pi) = \int_{-\pi}^{\pi} \frac{ds}{\omega - M\cos(s)} = 2\pi\sqrt{\frac{1}{\omega^2 - M^2}} > \frac{2\pi}{\omega}, \tag{60}$$

where we use the fact that $M < \omega$ (by (47)) and the integral

$$\int_0^z \frac{ds}{\omega - M\cos(s)} = 2\sqrt{\frac{1}{\omega^2 - M^2}} \arctan\left(\sqrt{\frac{\omega + M}{\omega - M}} \tan\left(\frac{z}{2}\right)\right), \quad z > 0.$$

For $Y^0 \in [0, kh - \mathfrak{e}]$, we have $dY/dt > 0$ for $X \in (0, \pi)$, and $dY/dt < 0$ when $X \in (-\pi, 0)$. If this streamline intersects the line $X = \frac{\pi}{2}$ at the value $Y = \mathcal{Y}$, then $(X(t), Y(t))$ lies below the line $Y = \mathcal{Y}$ for $X(t) \in [-\pi, -\frac{\pi}{2}) \cup (\frac{\pi}{2}, \pi]$, and lies above the line for $X(t) \in (-\frac{\pi}{2}, \frac{\pi}{2})$. Thus,

$$\dot{X} = M \cosh(Y) \cos(X) - \omega \geq M \cosh(\mathcal{Y}) \cos(X) - \omega, \quad t \geq 0. \tag{61}$$

Introducing the differential equation

$$\dot{\mathfrak{X}} = M \cosh(\mathcal{Y}) \cos(\mathfrak{X}) - \omega,$$

with $\mathfrak{X}(0) = \pi$, it follows immediately from (61) and the fact that $X(0) = \mathfrak{X}(0) = \pi$ that $X(t) \geq \mathfrak{X}(t)$ for $t \geq 0$. Therefore $t_{Y^0}(-\pi) > t^*$, where t^* is the time it takes for $\mathfrak{X}(t^*) = -\pi$. In a manner similar to solving (60), the value of t^* can be explicitly computed as being

$$t^* = 2\pi \sqrt{\frac{1}{\omega^2 - M^2 \cosh^2(\mathcal{Y})}} > \frac{2\pi}{\omega},$$

and hence $t_{Y^0}(-\pi) > \frac{2\pi}{\omega}$. This completes the proof.

The analysis of system (46) undertaken in Section 4.1, coupled with (58) and Theorem 5.2, facilitates a qualitative description of physical particle motion in the lower-fluid layer as prescribed by (44a). Assume a fluid particle is initially at its greatest depth $y(0) = y_0$: we label this position A. This corresponds to $X(0) = \pi$, and since $\dot{X} < 0$ along streamlines it follows that, in the moving frame, the variable $X(t)$ decreases continuously from π to $-\pi$, and we have: $\dot{x} < 0$, $\dot{y} > 0$ for $X(t) \in (\pi/2, \pi)$; $\dot{x} > 0$, $\dot{y} > 0$ for $X(t) \in (0, \pi/2)$; $\dot{x} > 0$, $\dot{y} < 0$ for $X(t) \in (-\pi/2, 0)$; $\dot{x} < 0$, $\dot{y} < 0$ for $X(t) \in (-\pi, -\pi/2)$; . The particle returns to its lowest position in the fluid layer (with depth $y = y_0$) at time $t = t_{Y^0}(-\pi) > 2\pi/\omega$, having experienced a positive horizontal drift: we label this position B.

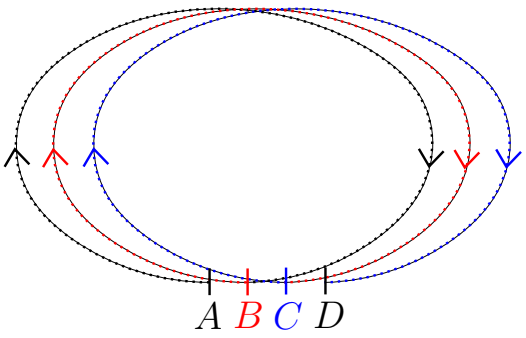


Figure 9: Schematic of a typical particle trajectory in the lower-fluid layer, representing its location at time: $t = 0$ (A); $t = t_{Y_0}(-\pi)$ (B); $t = 2t_{Y_0}(-\pi)$ (C); $t = 3t_{Y_0}(-\pi)$ (D).

Proposition 5.3 *The horizontal drift experienced by a fluid particle in the lower fluid layer over one wave period decreases strictly with depth.*

Proof The horizontal drift experienced by a fluid particle over one wave period is given by $D(Y^0) = x(t_{Y^0}(-\pi)) - x(\pi) = (\omega t_{Y^0}(-\pi) - 2\pi)/k > 0$, which can be expressed from (46a) as

$$D(Y^0) = 2\int_0^\pi \frac{M\cosh(Y)\cos(X)dX}{\omega - M\cosh(Y)\cos(X)}$$

Let $Y^1 < Y^0$, with $\tilde{Y} = \tilde{Y}(X)$ denoting the streamline for which $\tilde{Y}(\pi) = Y^1$.

$$D(Y^0) - D(Y^1) = 2\int_0^\pi \frac{\omega M\left(\cosh(Y) - \cosh(\tilde{Y})\right)\cos(X)}{(\omega - M\cosh(Y)\cos(X))\left(\omega - M\cosh(\tilde{Y})\cos(X)\right)}dX,$$

which, in the limit $Y^1 \to Y^0$, has the same sign as

$$\begin{aligned}\lim_{\tilde{Y}\to Y} 2\int_0^\pi \frac{\omega M\left(\cosh(Y) - \cosh(\tilde{Y})\right)\cos(X)}{(\omega - M\cosh(Y)\cos(X))\left(\omega - M\cosh(\tilde{Y})\cos(X)\right)(Y - \tilde{Y})}dX \\ = 2\int_0^\pi \frac{\omega M\cosh(Y)\cos(X)}{(\omega - M\cosh(Y)\cos(X))^2}dX > 2\int_0^\pi \frac{\omega M\cosh(Y)\cos(X)}{\omega^2}dX \\ > 2\int_0^\pi \frac{M}{\omega}\cosh(\mathcal{Y})\cos(X)dX = 0.\end{aligned}$$

Thus $D(Y^0) > D(Y^1)$, and the particle drift is decreasing with depth.

5.2 Upper-fluid layer

In the upper fluid layer the horizontal drift experienced by a fluid particle over one wave period is given by $D(Y_1^0) = x(t_{Y_1^0}(-\pi)) - x(\pi) = (\omega t_{Y_1^0}(-\pi) - 2\pi)/k > 0$, which can be expressed from (50) as

$$D(Y_1^0) = 2\int_0^\pi \frac{M_1 f(Y_1)\cos(X)dX}{\omega - M_1 f(Y_1)\cos(X)}.$$

If $Y_1^1 < Y_1^0$, where $\tilde{Y}_1 = \tilde{Y}_1(X)$ denotes the streamline with $\tilde{Y}_1(\pi) = Y_1^1$, then

$$D(Y_1^0) - D(Y_1^1) = 2\int_0^\pi \frac{\omega M_1 \left(f(Y_1) - f(\tilde{Y})\right)\cos(X)}{(\omega - M_1 f(Y_1)\cos(X))\left(\omega - M_1 f(\tilde{Y})\cos(X)\right)}dX.$$

In the limit $Y_1^1 \to Y_1^0$, the drift $D(Y_1^0) - D(Y_1^1)$ has the same sign as

$$\begin{aligned}\lim_{\tilde{Y}_1 \to Y_1} 2\int_0^\pi &\frac{\omega M_1 \left(f(Y_1) - f(\tilde{Y}_1)\right)\cos(X)}{(\omega - M_1 f(Y_1)\cos(X))\left(\omega - M_1 f(\tilde{Y}_1)\cos(X)\right)(Y_1 - \tilde{Y}_1)}dX \\ = 2\int_0^\pi &\frac{\omega M_1 f'(Y_1)\cos(X)}{(\omega - M_1 f(Y_1)\cos(X))^2}dX = 2\int_0^\pi \frac{\omega M_1 g(Y_1)\cos(X)}{(\omega - M_1 f(Y_1)\cos(X))^2}dX. \quad (62)\end{aligned}$$

As with the phase-plane analysis of Section 4.2, the qualitative behaviour of fluid particles in the upper-layer is markedly different depending on the parameter values $A < 1$, $A = 1$, $A > 1$. We deal with these cases separately.

5.2.1 $A > 1$

Although streamline patterns in the moving frame are more varied for the parameter value $A > 1$, it turns out that the behaviour of fluid particle trajectories in this regime is the simplest to describe. We state our main result as follows.

Theorem 5.4 *Let $A > 1$. There are no closed particle paths in the upper-fluid layer whose motion is governed by the system* (44b)*. That is, the system* (44b) *has no solutions $(x(t), y(t))$ which are periodic.*

Proof With reference to Figure 8, streamlines of the upper-fluid layer are restricted to the phase-portrait region for which $Y_1^0 \in [\mathfrak{e}_1, kh_1 + \mathfrak{e}]$. There is a change in the qualitative behaviour of streamlines depending on whether $kh_1 < \bar{Y}_1$ or $kh_1 > \bar{Y}_1$, where $\bar{Y}_1$ is prescribed by (56), and so we address these scenarios separately.

Case 1: $kh_1 \leq \bar{Y}_1$. In this setting the surface and internal wave are in-phase. First assume that $Y_1^0 < \bar{Y}_1$: along all such streamlines we have $dY_1/dt < 0$ for $X \in (0, \pi)$, and $dY_1/dt > 0$ when $X \in (-\pi, 0)$. Fixing a streamline, and supposing it intersects the line $X = \frac{\pi}{2}$ at $Y_1 = \mathcal{Y}_1$, then we deduce that $(X(t), Y_1(t))$ lies below the line $Y_1 = \mathcal{Y}_1$ for $X(t) \in (-\frac{\pi}{2}, \frac{\pi}{2})$, and lies above the line for $X(t) \in [-\pi, -\frac{\pi}{2}) \cup (\frac{\pi}{2}, \pi]$. Using the monotonicity properties of $f(Y_1)$ for $Y_1 \leq \bar{Y}_1$ (cf. Figure 7) we infer that

$$\dot{X} = M_1 f(Y_1)\cos(X) - \omega \geq M_1 f(\mathcal{Y}_1)\cos(X) - \omega, \quad t \geq 0. \tag{63}$$

Noting the similarities between inequalities (61) and (63), the subsequent arguments used in the proof of Theorem 5.2 carry over here (applied now to the differential equation $\dot{\mathfrak{X}} = M_1 f(\mathcal{Y}_1)\cos(\mathfrak{X}) - \omega$) and we deduce that $t_{Y_1^0}(-\pi) > t^*$, with

$$t^* = 2\pi\sqrt{\frac{1}{\omega^2 - M_1^2 f^2(\mathcal{Y}_1)}} > \frac{2\pi}{\omega}.$$

For the case $Y_1 = \bar{Y}_1$, in which the streamline is the flat 0−isocline, we note that $f(Y_1) \equiv f(\mathcal{Y}_1) \equiv f(\bar{Y}_1)$ and the inequality in relation (63) becomes an equality, leading to

$$t_{\bar{Y}_1}(-\pi) = t^* = 2\pi\sqrt{\frac{1}{\omega^2 - M_1^2 f^2\left(\bar{Y}_1\right)}} > \frac{2\pi}{\omega}.$$

Case 2: $kh_1 > \bar{Y}_1$. In this setting the surface and internal waves are out-of-phase, and the upper-fluid layer comprises two regions with qualitatively disparate streamlines. The first region consists of streamlines where $Y_1^0 \in [\mathfrak{e}_1, \bar{Y}_1)$ (and so includes the free-surface): the argumentation employed in Case 1, above, is applicable to this region, and so $t_{Y_1^0}(-\pi) > \frac{2\pi}{\omega}$ for these streamlines. The second region is composed of streamlines for which $Y_1^0 \in (\bar{Y}_1, kh_1 + \mathfrak{e}]$ (and includes the internal interface): these regions are separated by the flat 0−isocline streamline $Y = \bar{Y}_1$. Streamlines in the second region are 'out-of-phase' from those in the first, in the sense that there is a reversal in the vertical direction of motion, meaning that $dY_1/dt > 0$ for $X \in (0, \pi)$ and $dY_1/dt < 0$ for $X \in (-\pi, 0)$. Once more we fix a streamline, and let $Y_1 = \mathcal{Y}_1$ denote the location where this streamline intersects $X = \frac{\pi}{2}$. We observe that the streamline now lies above $Y_1 = \mathcal{Y}_1$ for $X(t) \in (-\frac{\pi}{2}, \frac{\pi}{2})$, and lies below this line for $X(t) \in [-\pi, -\frac{\pi}{2}) \cup (\frac{\pi}{2}, \pi]$. However, there is also a reversal in the monotonicity properties of $f(Y_1)$ for $Y_1 > \bar{Y}_1$ (cf. Figure 7), and so inequality (63) applies also to streamlines in this region. Repeating

the subsequent arguments of Case 1, above, enables us to conclude that $t_{Y_1^0}(-\pi) > t^* > \frac{2\pi}{\omega}$ in this second streamline region.

The qualitative nature of fluid particle trajectories in the upper-fluid layer prescribed by (44b) when $A > 1$ can now be determined from the analysis of system (50) performed in Section 4.2, coupled with transformation (59) and Theorem 5.4. Note that, along streamlines in the moving frame, $\dot{X}(t) < 0$ for solutions of system (50): $X(t)$ decreases continuously from $X = \pi$ to reach $X = -\pi$ in time $t_{Y_1^0}(-\pi)$.

For the sake of generality, we assume that $kh_1 > \bar{Y_1}$: if the alternative is true, simply restrict attention to streamlines with $Y_1^0 \in [\mathfrak{e}_1, \bar{Y_1})$ in this discussion. For streamlines in this region (which corresponds physically to the top section of the upper-fluid layer) we have: $\dot{x} < 0$, $\dot{y} > 0$ for $X(t) \in (\pi/2, \pi)$; $\dot{x} > 0$, $\dot{y} > 0$ for $X(t) \in (0, \pi/2)$; $\dot{x} > 0$, $\dot{y} < 0$ for $X(t) \in (-\pi/2, 0)$; $\dot{x} < 0$, $\dot{y} < 0$ for $X(t) \in (-\pi, -\pi/2)$. Fluid particles in this region return to their lowest position in the fluid layer, with depth $y = y_0$, say, after the time $t_{Y_1^0}(-\pi)$, having experienced a forward horizontal drift $x(t_{Y_1^0}(-\pi)) - x(0) = \left(t_{Y_1^0}(-\pi)\omega - 2\pi\right)/k > 0$. This particle motion is captured in schematic (a) of Figure 10.

At the 0−isocline $Y = \bar{Y_1}$ the motion is given by $\dot{x} < 0$ for $X(t) \in (\pi/2, \pi)$; $\dot{x} > 0$ for $X(t) \in (0, \pi/2)$; $\dot{x} > 0$ for $X(t) \in (-\pi/2, 0)$; $\dot{x} < 0$ for $X(t) \in (-\pi, -\pi/2)$. Fluid particles located on the 0−isocline experience a forward horizontal drift $x(t_{\bar{Y_1}}(-\pi)) - x(0) = (t_{\bar{Y_1}}(-\pi)\omega - 2\pi)/k > 0$. This motion is represented by schematic (b) of Figure 10.

For streamlines with $Y_1^0 \in (\bar{Y_1}, kh_1 + \mathfrak{e}]$ (which corresponds physically to the bottom region of the upper-fluid layer) we get: $\dot{x} < 0$, $\dot{y} < 0$ for $X(t) \in (\pi/2, \pi)$; $\dot{x} > 0$, $\dot{y} < 0$ for $X(t) \in (0, \pi/2)$; $\dot{x} > 0$, $\dot{y} > 0$ for $X(t) \in (-\pi/2, 0)$; $\dot{x} < 0$, $\dot{y} > 0$ for $X(t) \in (-\pi, -\pi/2)$. Fluid particles in this region return to their highest position in the fluid layer, with depth $y = y_0$, say, after the time $t_{Y_1^0}(-\pi)$, having experienced a forward horizontal drift $x(t_{Y_1^0}(-\pi)) - x(0) = \left(t_{Y_1^0}(-\pi)\omega - 2\pi\right)/k > 0$. This particle motion is depicted in schematic (c) of Figure 10.

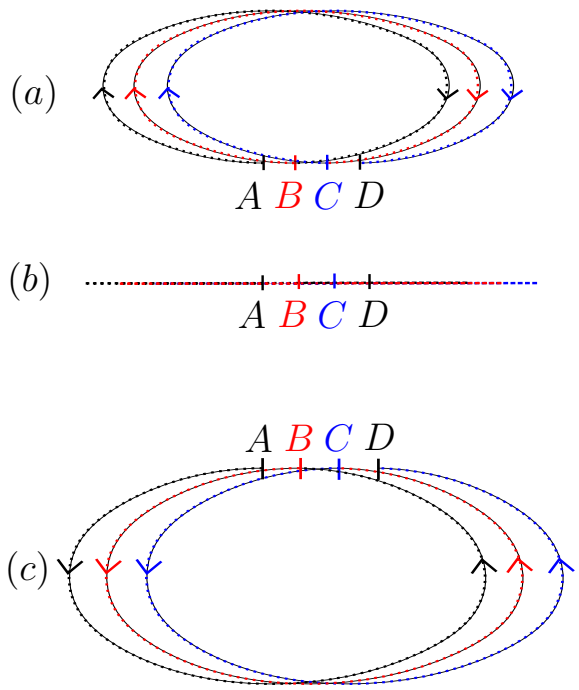


Figure 10: Schematics of typical trajectories for particles (a), (b), and (c) in the upper-fluid layer, for $A > 1$ and assuming that $kh_1 > \bar{Y}_1$. Their location at times $t = 0, t_{Y_1^0}(-\pi), 2t_{Y_1^0}(-\pi), 3t_{Y_1^0}(-\pi)$ are denoted by A, B, C, D, respectively.

Proposition 5.5 *Suppose $A > 1$. The horizontal drift experienced by a fluid particle in the upper fluid layer over one wave period decreases with depth for fluid motion of the type illustrated in schematic (a) of Figure 10, while it increases with depth for fluid motion of the type illustrated in schematic (c) of Figure 10. Accordingly, the minimum horizontal drift experienced by fluid particles occurs at $Y = \bar{Y}_1$, as illustrated in schematic (b) of Figure 10.*

Proof In the setting $A > 1$, along streamlines for which $Y_1^0 \in [\mathfrak{e}_1, \bar{Y}_1)$, the function $f(Y_1)$ is positive and monotonically decreasing, while $g(Y_1)$ is negative and monotonically increasing. Hence, from (62), the drift $D(Y_1^0) - D(Y_1^1)$ has the same sign as

$$2\int_0^\pi \frac{\omega M_1 g(Y_1)\cos(X)}{\left(\omega - M_1 f(Y_1)\cos(X)\right)^2} dX < 2\int_0^\pi \frac{\omega M_1 g(Y_1)\cos(X)}{\omega^2} dX$$
$$< 2\int_0^\pi \frac{M_1}{\omega} g(\mathcal{Y}_1)\cos(X) dX = 0.$$

Thus $D(Y_1^0) > D(Y_1^1)$ and, in terms of physical variables, the particle drift is decreasing with depth along these streamlines. Along streamlines for which $Y_1^0 \in (\bar{Y_1}, kh_1 + \mathfrak{e}]$, the function $f(Y_1)$ is positive and monotonically increasing, while $g(Y_1)$ is positive and monotonically increasing. By (62), the drift $D(Y_1^0) - D(Y_1^1)$ has the same sign as

$$2\int_0^\pi \frac{\omega M_1 g(Y_1)\cos(X)}{\left(\omega - M_1 f(Y_1)\cos(X)\right)^2} dX > 2\int_0^\pi \frac{\omega M_1 g(Y_1)\cos(X)}{\omega^2} dX$$
$$> 2\int_0^\pi \frac{M_1}{\omega} g(\mathcal{Y}_1)\cos(X) dX = 0.$$

Thus $D(Y_1^0) < D(Y_1^1)$ and, in terms of physical variables, the particle drift is increasing with depth along these streamlines. It follows that the minimum horizontal drift experienced by fluid particles must occur at the $0-$isocline $Y = \bar{Y_1}$.

5.2.2 $A = 1$

Due to the straightforward form that the functions $f(Y_1), g(Y_1)$ assume in the setting $A = 1$, a comprehensive qualitative description of fluid motion can be achieved.

Theorem 5.6 *Let $A = 1$. There are no closed particle paths in the upper-fluid layer whose motion is governed by the system* (44b).

Proof For $A = 1$ we have $f(Y_1) = e^{-Y_1} = -g(Y_1)$, and it can easily be shown that the analogue of inequality (63) holds for streamlines in the region $Y_1^0 \in [\mathfrak{e}_1, kh_1 + \mathfrak{e}]$. Consequently,

$$t_{Y_1^0}(-\pi) > 2\pi\sqrt{\frac{1}{\omega^2 - M_1^2 f^2(\mathcal{Y}_1)}} > \frac{2\pi}{\omega}.$$

It follows immediately that: $\dot{x} < 0$, $\dot{y} > 0$ for $X(t) \in (\pi/2, \pi)$; $\dot{x} > 0$, $\dot{y} > 0$ for $X(t) \in (0, \pi/2)$; $\dot{x} > 0$, $\dot{y} < 0$ for $X(t) \in (-\pi/2, 0)$; $\dot{x} < 0$, $\dot{y} < 0$ for $X(t) \in (-\pi, -\pi/2)$. Fluid particle motion matches that illustrated in schematic (a) of Figure 10, with all fluid particles experiencing a forward drift.

Proposition 5.7 *Suppose $A = 1$. The horizontal drift experienced by a fluid particle in the upper fluid layer over one wave period is decreasing with depth.*

Proof In this setting $f(Y_1)$ is positive and monotonically decreasing, while $g(Y_1)$ is negative and monotonically increasing. Thus, as in the first part of the proof of Proposition 5.5 above, $D(Y_1^0) > D(Y_1^1)$, and the particle drift is decreasing with depth in terms of physical variables.

5.2.3 $A < 1$

Although the phase-portrait for the streamlines appears more straightforward when $A < 1$, it turns out that particle motion is more convoluted and intricate in this case than for $A > 1$.

Theorem 5.8 *Let $A < 1$. There are no closed particle paths in the upper-fluid layer whose motion is governed by the system* (44b).

Proof In this setting, $f(Y_1)$ is monotonically decreasing (cf. Figure 4) and along streamlines we have $dY_1/dt < 0$ for $X \in (0, \pi)$, and $dY_1/dt > 0$ when $X \in (-\pi, 0)$ (cf. Figure 5). Fix a streamline by choosing $Y_1^0 \in [\mathfrak{e}_1, kh_1 + \mathfrak{e}]$, and suppose it intersects $X = \frac{\pi}{2}$ at $Y_1 = \mathcal{Y}_1$, then it follows as before that

$$\dot{X} = M_1 f(Y_1)\cos(X) - \omega \geq M_1 f(\mathcal{Y}_1)\cos(X) - \omega, \quad t \geq 0.$$

As in the proof of Theorem 5.4, we deduce that $t_{Y_1^0}(-\pi) > t^*$, with

$$t^* = 2\pi\sqrt{\frac{1}{\omega^2 - M_1^2 f^2(\mathcal{Y}_1)}} > \frac{2\pi}{\omega}.$$

For $A < 1$ there is a change in the qualitative behaviour of particle motion associated with the change in sign of $f(Y_1)$ that potentially occurs at $Y_1 = \bar{Y}_1$, as seen in Figure 4. We therefore consider separately the fluid motion for two distinct cases.

Case 1: $kh_1 + \mathfrak{e} \leq \bar{Y}_1$. In this regime, $f(Y_1)$ is positive and monotonically decreasing (cf. Figure 4) and $\dot{x} < 0$, $\dot{y} > 0$ for $X(t) \in (\pi/2, \pi)$; $\dot{x} > 0$, $\dot{y} > 0$ for $X(t) \in (0, \pi/2)$; $\dot{x} > 0$, $\dot{y} < 0$ for $X(t) \in (-\pi/2, 0)$; $\dot{x} < 0$, $\dot{y} < 0$ for $X(t) \in (-\pi, -\pi/2)$. Fluid particles in this region return to their lowest position in the fluid layer, with depth $y = y_0$, say, after the time $t_{Y_1^0}(-\pi)$, having experienced a forward horizontal drift $x(t_{Y_1^0}(-\pi)) - x(0) = \left(t_{Y_1^0}(-\pi)\omega - 2\pi\right)/k > 0$. This particle motion is captured in schematic (a) of Figure 11.

Case 2: $kh_1 + \mathfrak{e} > \bar{Y}_1$. In this case, along streamlines for which $Y_1^0 \leq \bar{Y}_1$, fluid particles will possess the same qualitative motion as discussed in Case 1, above, and illustrated in schematic (a) of Figure 11. There is a change in the sign of $f(Y_1)$ occurring when $Y_1 = \bar{Y}_1$.

Let us first suppose that $Y_1^0 > \bar{Y}_1$ defines a streamline which intersects $Y_1 = \bar{Y}_1$ at some value $\bar{X} \in (\pi/2, \pi)$ (and, by symmetry, $\bar{X} \in (-\pi, -\pi/2)$). Then we have the following motion: $\dot{x} > 0$, $\dot{y} > 0$ for $X(t) \in (\bar{X}, \pi)$; $\dot{x} < 0$, $\dot{y} > 0$ for $X(t) \in (\pi/2, \bar{X})$; $\dot{x} > 0$, $\dot{y} > 0$ for $X(t) \in (0, \pi/2)$; $\dot{x} > 0$, $\dot{y} < 0$

for $X(t) \in (-\pi/2, 0)$; $\dot{x} < 0$, $\dot{y} < 0$ for $X(t) \in (-\bar{X}, -\pi/2)$; $\dot{x} > 0$, $\dot{y} < 0$ for $X(t) \in (-\pi, -\bar{X})$. Particle trajectories which exhibit such motion are given in schematics (b) and (c) of Figure 11.

If $Y_1^0 > \bar{Y}_1$ is such that the streamline intersects $Y_1 = \bar{Y}_1$ at $\bar{X} = \pi/2$ (and $\bar{X} = -\pi/2$, by symmetry), then $\dot{x} > 0$ for $X(t) \in (-\pi, -\pi/2) \cup (-\pi/2, 0) \cup (0, \pi/2) \cup (\pi/2, \pi)$, and $\dot{y} > 0$ for $X(t) \in (0, \pi)$, with $\dot{y} < 0$ for $X(t) \in (-\pi, 0)$. Such a particle trajectory is illustrated in schematic (d) of Figure 11.

Suppose now that $Y_1^0 > \bar{Y}_1$ is such that the streamline intersects $Y_1 = \bar{Y}_1$ at $\bar{X} \in (0, \pi/2)$ (and, by symmetry, $\bar{X} \in (-\pi/2, 0)$), then we have the following motion: $\dot{x} > 0$, $\dot{y} > 0$ for $X(t) \in (\pi/2, \pi)$; $\dot{x} < 0$, $\dot{y} > 0$ for $X(t) \in (\bar{X}, \pi/2)$; $\dot{x} > 0$, $\dot{y} > 0$ for $X(t) \in (0, \bar{X})$; $\dot{x} > 0$, $\dot{y} < 0$ for $X(t) \in (-\bar{X}, 0)$; $\dot{x} < 0$, $\dot{y} < 0$ for $X(t) \in (-\pi/2, -\bar{X})$; $\dot{x} > 0$, $\dot{y} < 0$ for $X(t) \in (-\pi, -\pi/2)$. Examples of particle trajectories displaying such qualitative behaviour are given in schematics (e) and (f) of Figure 11.

Finally, for streamlines prescribed by $Y_1^0 > \bar{Y}_1$ which intersect $Y_1 = \bar{Y}_1$ at $\bar{X} = 0$, or which do not intersect $Y_1 = \bar{Y}_1$, the function $f(Y_1)$ is negative and monotonically decreasing, giving us the motion: $\dot{x} > 0$, $\dot{y} > 0$ for $X(t) \in (\pi/2, \pi)$; $\dot{x} < 0$, $\dot{y} > 0$ for $X(t) \in (0, \pi/2)$; $\dot{x} < 0$, $\dot{y} < 0$ for $X(t) \in (-\pi/2, 0)$; $\dot{x} > 0$, $\dot{y} < 0$ for $X(t) \in (-\pi, -\pi/2)$. A particle trajectory for this case is given in schematic (g) of Figure 11.

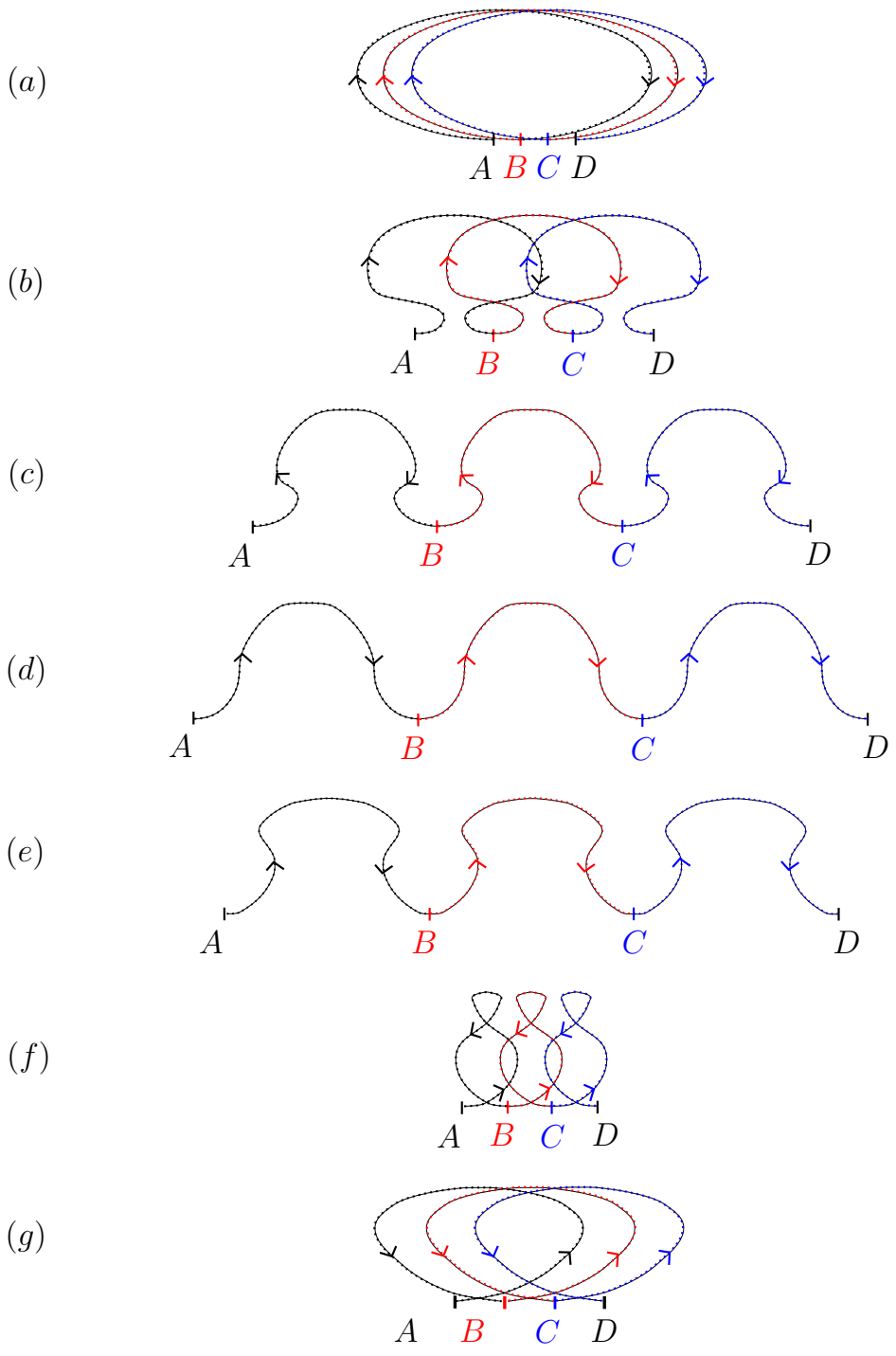


Figure 11: Schematics of typical trajectories for particles in the upper-fluid layer for $A < 1$, assuming that $kh_1 + \mathfrak{e} > \bar{Y}_1$. Their location at times $t = 0, t_{Y_1^0}(-\pi), 2t_{Y_1^0}(-\pi), 3t_{Y_1^0}(-\pi)$ are denoted by A, B, C, D, respectively.

Proposition 5.9 *Suppose $A < 1$. For fluid motion of the type illustrated in schematic (a) in Figure 11, the horizontal drift experienced by a fluid particle in the upper fluid layer over one wave period is decreasing with depth.For fluid motion of the type illustrated in schematic (g) in Figure 11, the horizontal drift experienced by a fluid particle over one wave period increases with depth.*

Proof In the setting $A < 1$, along streamlines for which $Y_1^0 \leq \bar{Y_1}$ the function $f(Y_1)$ is positive and monotonically decreasing, while $g(Y_1)$ is negative and monotonically increasing. Hence, from (62), the drift $D(Y_1^0) - D(Y_1^1)$ has the same sign as

$$2\int_0^\pi \frac{\omega M_1 g(Y_1)\cos(X)}{\left(\omega - M_1 f(Y_1)\cos(X)\right)^2} dX < 2\int_0^\pi \frac{\omega M_1 g(Y_1)\cos(X)}{\omega^2} dX$$
$$< 2\int_0^\pi \frac{M_1}{\omega} g(\mathcal{Y}_1)\cos(X) dX = 0.$$

Thus $D(Y_1^0) > D(Y_1^1)$ and, in terms of physical variables, the particle drift is decreasing with depth along these streamlines. These are the only streamlines which feature in the physical regime with $kh_1 + \mathfrak{e} \leq \bar{Y_1}$.

The setting $kh_1 + \mathfrak{e} > \bar{Y_1}$ encompasses streamlines whereby $Y_1^0 \leq \bar{Y_1}$: the above considerations apply directly to these streamlines. For the remaining streamlines in this setting, whereby $Y_1^0 > \bar{Y_1}$, consider either those which do not intersect $Y_1 = \bar{Y_1}$, or which intersect $Y_1 = \bar{Y_1}$ at the point $\bar{X} = 0$. For these streamlines, the function $f(Y_1)$ is negative and monotonically decreasing, as is the function $g(Y_1)$. Hence, by (62) the drift $D(Y_1^0) - D(Y_1^1)$ has the same sign as

$$2\int_0^\pi \frac{\omega M_1 g(Y_1)\cos(X)}{\left(\omega - M_1 f(Y_1)\cos(X)\right)^2} dX > 2\int_0^\pi \frac{\omega M_1 g(Y_1)\cos(X)}{\omega^2} dX$$
$$> 2\int_0^\pi \frac{M_1}{\omega} g(\mathcal{Y}_1)\cos(X) dX = 0.$$

Thus $D(Y_1^0) < D(Y_1^1)$ and, in terms of physical variables, the particle drift is increasing with depth along these streamlines.

Acknowledgements

DH would like to acknowledge the support of the Science Foundation Ireland (SFI) grant 13/CDA/2117.

References

[1] Werner Alpers. Theory of radar imaging of internal waves. *Nature*, 314:245–247, 1985.

[2] Jerry L. Bona, David Lannes, and Jean-Claud Saut. Asymptotic models for internal waves. *J. Math. Pures Appl. (9)*, 89(6):538–566, 2008.

[3] Adrian Constantin. The trajectories of particles in Stokes waves. *Invent. Math.*, 166(3):523–535, 2006.

[4] Adrian Constantin. *Nonlinear water waves with applications to wave-current interactions and tsunamis*, volume 81 of *CBMS-NSF Regional Conference Series in Applied Mathematics*. Society for Industrial and Applied Mathematics (SIAM), Philadelphia, PA, 2011.

[5] Adrian Constantin. Particle trajectories in extreme Stokes waves. *IMA J. Appl. Math.*, 77(3, SI):293–307, 2012.

[6] Adrian Constantin. The flow beneath a periodic travelling surface water wave. *J. Phys. A*, 48(14), 2015.

[7] Adrian Constantin, Mats Ehrnström, and Gabriele Villari. Particle trajectories in linear deep-water waves. *Nonlinear Anal. Real World Appl.*, 9(4):1336–1344, 2008.

[8] Adrian Constantin and Joachim Escher. Particle trajectories in solitary water waves. *Bull. Amer. Math. Soc.*, 44(3):423–431, 2007.

[9] Adrian Constantin and Rossen I. Ivanov. A Hamiltonian approach to wave-current interactions in two-layer fluids. *Phys. Fluids*, 27(8):086603, 2015.

[10] Adrian Constantin and Rossen I. Ivanov. Equatorial wave-current interactions. *Comm. Math. Phys.*, 370(1):1–48, 2019.

[11] Adrian Constantin, Rossen I. Ivanov, and Calin I. Martin. Hamiltonian formulation for wave-current interactions in stratified rotational flows. *Arch. Ration. Mech. Anal.*, 221(3):1417–1447, 2016.

[12] Adrian Constantin and Gabriele Villari. Particle trajectories in linear water waves. *J. Math. Fluid Mech.*, 10(1):1–18, 2008.

[13] Walter Craig, Philippe Guyenne, and Henrik Kalisch. Hamiltonian long-wave expansions for free surfaces and interfaces. *Comm. Pure Appl. Math.*, 58(12):1587–1641, 2005.

[14] Walter Craig, Philippe Guyenne, and Catherine Sulem. Coupling between internal and surface waves. *Nat. Haz.*, 57(3):617–642, 2011.

[15] Walter Craig, Philippe Guyenne, and Catherine Sulem. The surface signature of internal waves. *J. Fluid Mech.*, 710:277–303, 2012.

[16] Mats Ehrnström, Joachim Escher, and Gabriele Villari. Steady water waves with multiple critical layers: interior dynamics. *J. Math. Fluid Mech.*, 14(3):407–419, 2012.

[17] Mats Ehrnström and Gabriele Villari. Linear water waves with vorticity: rotational features and particle paths. *J. Differential Equations*, 244(8):1888–1909, 2008.

[18] C Garrett and W Munk. Internal waves in the ocean. *Ann. Rev. Fluid Mech.*, 11(1):339–369, 1979.

[19] Jessica C. Garwood, Ruth C. Musgrave, and Andrew J. Lucas. Life in internal waves. *Oceanography*, 33, 2020.

[20] Karl R. Helfrich and W. Kendall Melville. Long nonlinear internal waves. *Ann. Rev. Fluid Mech.*, 38(1):395–425, 2006.

[21] David Henry. The trajectories of particles in deep-water Stokes waves. *Int. Math. Res. Not.*, pages Art. ID 23405, 13, 2006.

[22] David Henry. Particle trajectories in linear periodic capillary and capillary-gravity deep-water waves. *J. Nonlinear Math. Phys.*, 14(1):1–7, 2007.

[23] David Henry. Particle trajectories in linear periodic capillary and capillary-gravity water waves. *Philos. Trans. R. Soc. A*, 365(1858):2241–2251, 2007.

[24] David Henry. On the deep-water Stokes wave flow. *Int. Math. Res. Not.*, pages Art. ID rnn 071, 7, 2008.

[25] David Henry. Steady periodic flow induced by the Korteweg-de Vries equation. *Wave Motion*, 46(6):403–411, 2009.

[26] David Henry. Stokes drift in equatorial water waves, and wave–current interactions. *Deep Sea Res. Part II*, 160:41–47, 2019.

[27] Delia Ionescu-Kruse. Small-amplitude capillary-gravity water waves: exact solutions and particle motion beneath such waves. *Nonlinear Anal. Real World Appl.*, 11(4):2989–3000, 2010.

[28] Delia Ionescu-Kruse. On the particle paths and the stagnation points in small-amplitude deep-water waves. *J. Math. Fluid Mech.*, 15(1):41–54, 2013.

[29] Delia Ionescu-Kruse and Anca-Voichita Matioc. Small-amplitude equatorial water waves with constant vorticity: dispersion relations and particle trajectories. *Discrete Contin. Dyn. Syst.*, 34(8):3045–3060, 2014.

[30] Blair Kinsman. *Wind Waves: Their Generation and Propagation on the Ocean Surface*. Prentice-Hall, Englewood Cliffs, N.J., 1965.

[31] Horace Lamb. *Hydrodynamics*. Cambridge Mathematical Library. Cambridge University Press, Cambridge, sixth edition, 1993.

[32] Kevin G. Lamb. Internal wave breaking and dissipation mechanisms on the continental slope/shelf. *Ann. Rev. Fluid Mech.*, 46(1):231–254, 2014.

[33] David Lannes. *The water waves problem*, volume 188 of *Mathematical Surveys and Monographs*. American Mathematical Society, Providence, RI, 2013. Mathematical analysis and asymptotics.

[34] Michael S. Longuet-Higgins. The trajectories of particles in steep, symmetric gravity waves. *J. Fluid Mech.*, 94(3):497–517, 1979.

[35] Tony Lyons. Particle trajectories in extreme Stokes waves over infinite depth. *Discrete Contin. Dyn. Syst.*, 34(8):3095–3107, 2014.

[36] Anca-Voichita Matioc. On particle trajectories in linear water waves. *Nonlinear Anal. Real World Appl.*, 11(5):4275–4284, 2010.

[37] Anca-Voichita Matioc. On particle trajectories in linear deep-water waves. *Commun. Pure Appl. Anal.*, 11(4):1537–1547, 2012.

[38] James D. Meiss. *Differential dynamical systems*, volume 14 of *Mathematical Modeling and Computation*. Society for Industrial and Applied Mathematics (SIAM), Philadelphia, PA, 2007.

[39] John Milnor. *Morse theory*. Based on lecture notes by M. Spivak and R. Wells. Annals of Mathematics Studies, No. 51. Princeton University Press, Princeton, N.J., 1963.

[40] Ronald Quirchmayr. On irrotational flows beneath periodic traveling equatorial waves. *J. Math. Fluid Mech.*, 19(2):283–304, 2017.

[41] Bruce R. Sutherland. *Internal Gravity Waves*. Cambridge University Press, 2010.

[42] Alessandro Toffoli and Elzbieta M. Bitner-Gregersen. *Types of Ocean Surface Waves, Wave Classification*, pages 1–8. John Wiley & Sons, Ltd., 2017.

[43] Geoffrey K. Vallis. *Atmospheric and Oceanic Fluid Dynamics: Fundamentals and Large-Scale Circulation*. Cambridge University Press, 2 edition, 2017.

[44] Ton S. van den Bremer and Øyvind Breivik. Stokes drift. *Phil. Trans. Roy. Soc. A*, 376(2111):20170104, 2018.

David Henry, School of Mathematical Sciences, University College Cork, Cork, Ireland. *E-mail address:* d.henry@ucc.ie

Gabriele Villari, Dipartimento di Matematica e informatica "Ulisse Dini", Università degli Studi di Firenze, viale Morgagni, 67/A, 50137 Firenze, Italy. *E-mail address:* gabriele.villari@unifi.it